

# Single-molecule dynamics show a transient lipopolysaccharide transport bridge

<https://doi.org/10.1038/s41586-023-06709-x>

Lisa Törk<sup>1</sup>, Caitlin B. Moffatt<sup>1,2</sup>, Thomas G. Bernhardt<sup>3,4</sup>, Ethan C. Garner<sup>2</sup>✉ & Daniel Kahne<sup>1,2</sup>✉

Received: 25 July 2022

Accepted: 4 October 2023

Published online: 8 November 2023

 Check for updates

Gram-negative bacteria are surrounded by two membranes. A special feature of the outer membrane is its asymmetry. It contains lipopolysaccharide (LPS) in the outer leaflet and phospholipids in the inner leaflet<sup>1–3</sup>. The proper assembly of LPS in the outer membrane is required for cell viability and provides Gram-negative bacteria intrinsic resistance to many classes of antibiotics. LPS biosynthesis is completed in the inner membrane, so the LPS must be extracted, moved across the aqueous periplasm that separates the two membranes and translocated through the outer membrane where it assembles on the cell surface<sup>4</sup>. LPS transport and assembly requires seven conserved and essential LPS transport components<sup>5</sup> (LptA–G). This system has been proposed to form a continuous protein bridge that provides a path for LPS to reach the cell surface<sup>6,7</sup>, but this model has not been validated in living cells. Here, using single-molecule tracking, we show that Lpt protein dynamics are consistent with the bridge model. Half of the inner membrane Lpt proteins exist in a bridge state, and bridges persist for 5–10 s, showing that their organization is highly dynamic. LPS facilitates Lpt bridge formation, suggesting a mechanism by which the production of LPS can be directly coupled to its transport. Finally, the bridge decay kinetics suggest that there may be two different types of bridges, whose stability differs according to the presence (long-lived) or absence (short-lived) of LPS. Together, our data support a model in which LPS is both a substrate and a structural component of dynamic Lpt bridges that promote outer membrane assembly.

How LPS, a molecule with six fatty acyl chains and tens to hundreds of sugars, can move rapidly from the inner membrane to the outer leaflet of the outer membrane through the aqueous periplasmic space has been a longstanding question. Lpt bridges have been proposed to explain how LPS is transported. In this model, LptB<sub>2</sub>FG comprises an ABC transporter that uses ATP hydrolysis to power the movement of LPS to the periplasmic domain of LptF, and from there over a bridge formed by the inner membrane-anchored LptC and periplasmic LptA proteins to the periplasmic domain of the outer membrane protein LptD<sup>8–15</sup> (Fig. 1a). Together with LptE, the β-barrel domain of LptD serves as a translocon to move LPS across the outer membrane and into the outer leaflet<sup>16–20</sup>. Although Lpt bridges have been shown to form *in vitro*<sup>7</sup>, they have not been shown to exist in living cells.

Single-molecule tracking provides a powerful tool for visualizing protein localization and dynamics in living cells<sup>21–25</sup> and we thought it might enable visualization of Lpt bridges<sup>26</sup>. Outer membrane proteins diffuse slowly within the membrane bilayer owing to the strong lateral interactions between LPS molecules<sup>27–30</sup>. By contrast, inner membrane proteins diffuse freely within the phospholipid bilayer<sup>31,32</sup>. If Lpt bridges indeed form in cells, then Lpt inner membrane proteins would be expected to enter a state in which they display slowed dynamics similar to those of outer membrane proteins.

## Lpt proteins have varying dynamic states

To visualize Lpt protein dynamics, we fused selected Lpt proteins to a HaloTag, a modified dehalogenase engineered to form covalent attachments to fluorophores containing a chloroalkane linker. Cells expressing Lpt-Halo fusion proteins in place of the endogenous Lpt protein were viable and displayed similar growth rates to wild-type cells (Extended Data Fig. 1f). To observe the motion of single Lpt proteins, we sparsely labelled the fusion proteins using low concentrations of the membrane-permeable Janelia Fluor HaloTag 549<sup>33,34</sup>. Total internal reflection microscopy was used to resolve single-molecule tracks that describe the xy positions of the protein in Cartesian coordinates (Fig. 1b,c), enabling us to specifically resolve the dynamics of single molecules within or associated with the relevant membranes. The two soluble proteins LptA and LptB are detected only when they are bound to a membrane-embedded protein with our acquisition rate<sup>35</sup>. To characterize the type of lateral motions exhibited by each of these labelled proteins, we monitored the area that the proteins sampled in a given amount of time—that is, their confinement radius. For this measurement, we calculated the average xy position (the centroid, blue point) from the xy position (black points) of each time point within a track (Fig. 1d). The confinement radius is defined as the average of the distances between the blue point and the black points. For each labelled

<sup>1</sup>Department of Chemistry and Chemical Biology, Harvard University, Cambridge, MA, USA. <sup>2</sup>Department of Molecular and Cellular Biology, Harvard University, Cambridge, MA, USA.

<sup>3</sup>Department of Microbiology, Blavatnik Institute, Harvard Medical School, Boston, MA, USA. <sup>4</sup>Howard Hughes Medical Institute, Boston, MA, USA. ✉e-mail: egarner@g.harvard.edu; Kahne@chemistry.harvard.edu

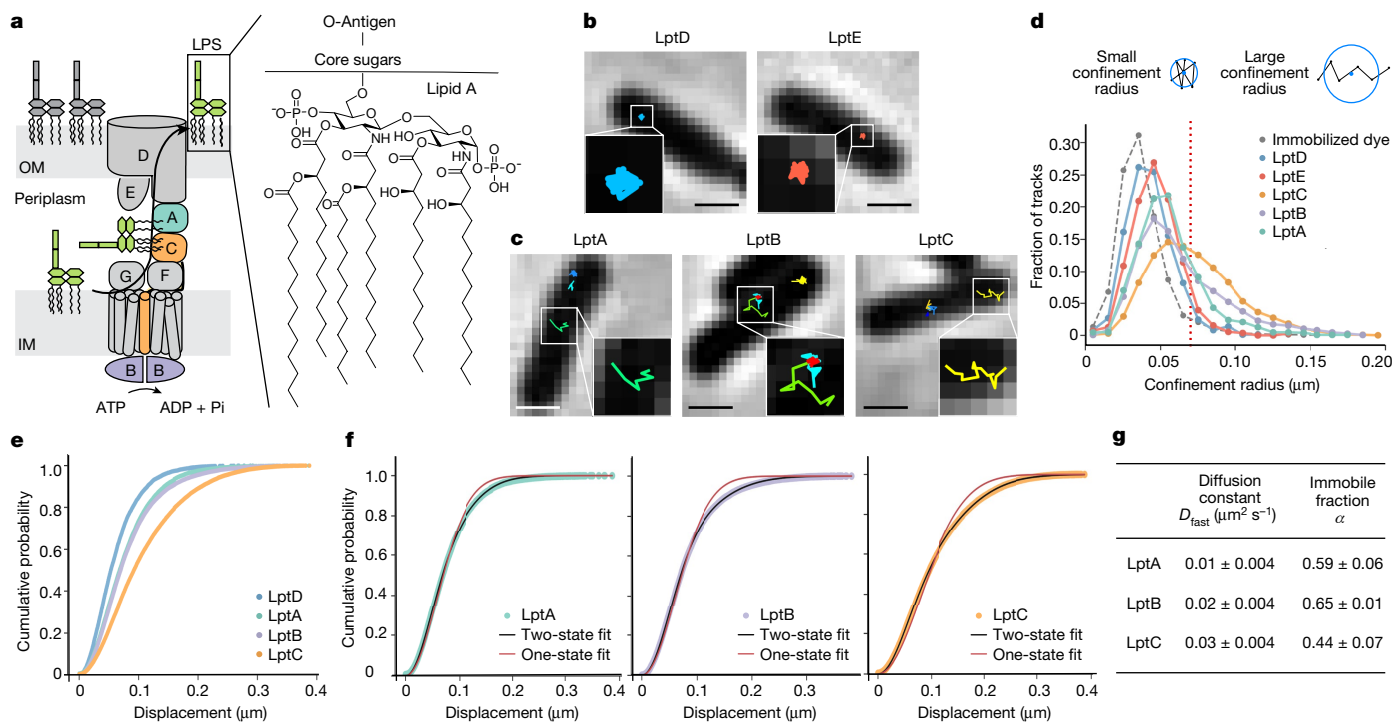


**Fig. 1 | Observation of an immobile state of Lpt proteins suggests that they can form a bridge in cells.** **a**, Schematic depicting the bridge model of LPS transport. IM, inner membrane; OM, outer membrane. **b, c**, Representative single-molecule tracks of LptD–Halo (strain LT18) and Halo–LptE (strain LT63) (**b**), and LptA–Halo (strain LT23), Halo–LptB (strain LT17) and Halo–LptC (strain LT16) (**c**). Each single-molecule track is shown in a different colour and overlaid over the corresponding phase-contrast image. Further representative trajectory images are shown in Extended Data Fig. 2. Representative single-molecule videos are presented in supplementary materials. Scale bars, 1  $\mu\text{m}$ . **d**, Top, schematic depicting the confinement radius measurement (the blue dot is the centroid of the track and the black dots show Cartesian coordinates of the track). Bottom, confinement radii histograms for the imaged Lpt protein tracks compared with the confinement radii histogram for immobilized dye,

which serves as a localization precision control. Dye:  $n = 4,836$ , LptA:  $n = 1,250$ , LptB:  $n = 2,964$ , LptC:  $n = 4,675$ , LptD:  $n = 855$  and LptE:  $n = 1,092$ . The results are representative of at least two independent experiments. Tracks with a confinement radius up to 0.07  $\mu\text{m}$  (red dotted line) are considered immobile. **e**, CDF of displacements with  $\Delta t = 200$  ms for single-molecule tracks of LptA, LptB, LptC and LptD. **f**, One-state (red line) and two-state (black line) dynamic models were fit to the CDF plots of LptA, LptB and LptC. **g**, The average diffusion constant,  $D_{\text{fast}}$ , and alpha values (immobile fraction) with standard deviations for LptA, LptB and LptC. These values result from the two-state dynamic model fit to the CDF plots. Residual plots are shown in Extended Data Fig. 4. Sample sizes for the CDF plots and all fit values are reported in Supplementary Table 5.

protein, we binned the confinement radii and plotted the frequency of the binned radii to visualize their dynamics. All imaged Lpt proteins contained a population with similar dynamics to an immobilized dye control that defined the slowest detectable dynamic state (the immobile state). The confinement radii plots of LptD and LptE were very similar to each other and resembled the dye control, consistent with previous studies showing that proteins in the outer membrane have highly restricted mobility<sup>26–30</sup>. By contrast, the confinement radius analysis showed a more complex dynamic profile for the periplasmic protein LptA and the inner membrane proteins LptB and LptC (Fig. 1d). The histograms of LptB and LptC displayed a shift in their maxima to larger confinement radii with longer distribution tails than LptD and LptE, indicating that they have greater mobility. A histogram of the confinement radii of LptA is also shifted to the right compared to LptD and LptE, but the frequency of trajectories dropped sharply as the confinement radius increased. Therefore, LptA is more mobile than LptD and LptE, but less mobile than LptB and LptC.

We carried out a cumulative distribution function (CDF) analysis for LptA, LptB and LptC to better define their dynamic states<sup>36</sup>. The CDF curve for LptD was shifted furthest to the left, showing small displacements. By contrast, the CDF curves of LptA, LptB and LptC were shifted to the right, consistent with their greater mobility (Fig. 1e). We fit the respective CDF curves with a one-state dynamic model and a two-state dynamic model (Fig. 1f). For all three proteins, the two-state model fits the data better (residual plots in Extended Data Fig. 4), implying

that LptA, LptB and LptC exist in at least two different dynamic states (Fig. 1g). For all three proteins, the slow dynamic state exhibited lower mobility than our fixed dye control (Fig. 1d), consistent with an immobile state resulting from connections of LptA, LptB and LptC to the outer membrane LptD and LptE proteins.

## Seven Lpt proteins form bridges in vivo

We next investigated whether the immobile state observed for LptA, LptB and LptC indeed reflects a bridge involving all seven proteins. To address this question, we took advantage of the LptC variant LptC(G153R)<sup>37,38</sup> (LptC\*, Fig. 2), which can bind to LptB<sub>2</sub>FG but is unable to interact with LptA to form a bridge (Fig. 2a). If the observed immobile state corresponds to transenvelope bridges, we would expect the production of untagged LptC\* to decrease the fraction of inner membrane complexes adopting the immobile state. Confinement radius plots of Halo–LptC in cells with increasing induction of LptC\* show a shift to a highly mobile state (Fig. 2b), suggesting that the immobile state of LptC indeed depends on connection of the inner membrane complex to the outer membrane Lpt proteins through LptA. The same behaviour was observed for Halo–LptB (Fig. 2c). The immobile fractions of Halo–LptC and Halo–LptB decreased below 10% when LptC\* was overproduced. The immobile fraction of LptA–Halo exhibited a different behaviour. The immobile fraction of LptA–Halo was higher than that of LptB and LptC under low LptC\* production levels and

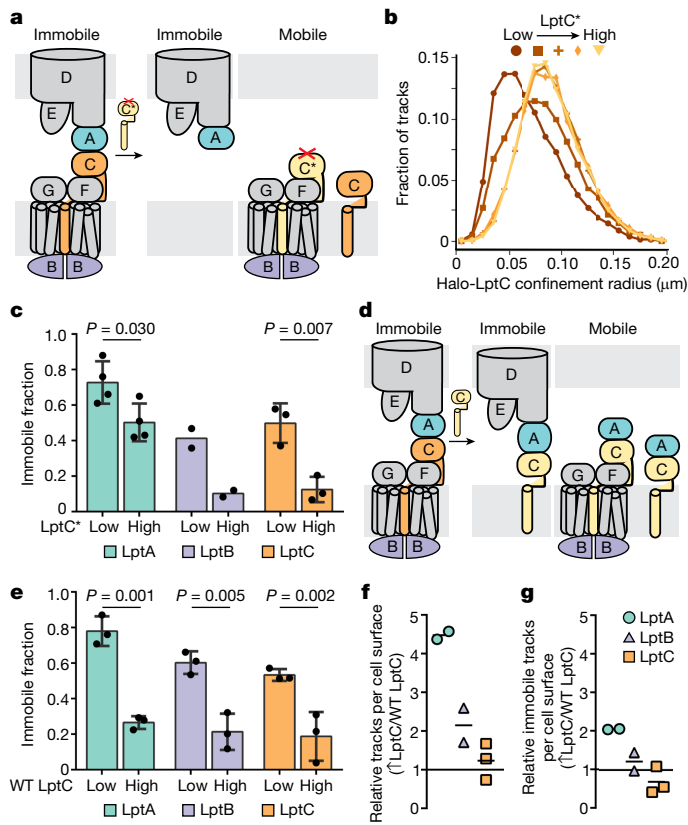


**Fig. 2 | LptA has immobile states that are independent of the bridging state, whereas LptB does not.** **a**, Schematic depicting breaking of Lpt bridges upon induction of LptC(G153R) (LptC\* or C\*), which cannot form bridges in cells. **b**, Confinement radius plots of Halo–LptC tracks measured with increasing amounts of LptC\*, induced with 0, 1, 7, 20, or 40 mM of arabinose. From low to high LptC\*: n = 5,142, 7,292, 12,660, 7,671 and 13,546. The result is representative of two independent experiments. **c**, **e**, Immobile fractions of single-molecule LptA, LptB and LptC tracks, imaged with (high) or without (low) inducing LptC\* (**c**) or wild-type LptC (**e**) production with 40 mM arabinose. The bar depicts the mean of independent experiments. Independent experiments are depicted as dots. The immobile fraction  $\alpha$  is obtained from the CDF fit. Pvalues were obtained from an independent two-sided t-test. **c**, LptA, LptC\* low: 7,926/4; LptA, LptC\* high: 25,407/4; LptB, LptC\* low: 9,603/2; LptB, LptC\* high: 16,488/2; LptC, LptC\* low: 30,847/3; LptC, LptC\* high: 47,101/3 (trajectories/independent experiments). **e**, LptA, LptC low: 14,300/3; LptA, LptC high: 44,086/3; LptB, LptC low: 6,407/3; LptB, LptC high: 15,591/3; LptC, LptC low: 11,427/3; LptC, LptC high: 14,076/3 (trajectories/independent experiments). CDF fit values and trajectory sample sizes are given in Supplementary Table 5. Corresponding confinement radius plots for the tracks can be found in Extended Data Fig. 5c,d. **d**, Schematic depicting the hypothesized effect of overproduction of wild-type LptC. **f**, The quotient of LptA, LptB and LptC tracks per cell surface with LptC overproduction and LptA, LptB and LptC tracks per cell surface under wild-type conditions. **g**, The quotient of immobile LptA, LptB and LptC tracks per cell surface with overproduction of wild-type LptC and immobile LptA, LptB and LptC tracks per cell surface under wild-type conditions. **f**, **g**, The average of the respective independent experiments is depicted as a line. An average quotient higher than 1 indicates an increase in tracks per cell (**f**) or immobile tracks per cell (**g**), and an average quotient of less than 1 indicates a decrease upon overproduction of LptC. Values for tracks per cell and immobile tracks per cell for each condition and time-lapse are provided in Supplementary Table 6.

remained higher when LptC\* production increased (Fig. 2c). A simple interpretation for the higher fraction of immobile LptA–Halo is that a substantial fraction remains associated with the outer membrane proteins LptDE when bridges are broken (Fig. 2a). Consistent with this interpretation, fractionation of cells showed that LptA is found largely

in the outer membrane fraction with LptD and LptE<sup>6</sup> (Extended Data Fig. 5e). Nevertheless, the fraction of immobile LptA decreased with expression of LptC\*, implying that there is a mobile state of LptA when the bridges are broken.

### LptB reports on the abundance of bridges

Because soluble LptA cannot be detected owing to its rapid diffusion in the periplasm<sup>35</sup>, we hypothesized that the mobile state of LptA that is observed when LptC\* is expressed represents LptA connected to endogenous wild-type LptC in the inner membrane complex. If some LptA indeed binds LptC, and if LptC is a limiting component of the bridge, one would predict that overexpressing wild-type LptC would lead to an increase in the mobile state of LptA because more soluble LptA would be recruited to the membrane where it can be detected. To test this possibility, we overexpressed wild-type LptC and monitored the dynamics of Halo-tagged LptA, LptB and LptC (Fig. 2d). The immobile fraction of all three proteins decreased, implying that more mobile inner membrane complexes form when LptC is overproduced. We measured the total number of resolvable tracks for Halo-tagged LptA, LptB and LptC when wild-type LptC was overproduced and normalized them to the number of tracks found in cells with endogenous levels of LptC (Fig. 2f). The number of total tracks per cell for Halo–LptC did not change, because all of its states (immobile and diffusing along the membrane) are observable. However, for LptA–Halo and Halo–LptB, the normalized number of tracks per cell increased, consistent with the recruitment of excess soluble LptA and LptB to the inner membrane upon LptC overproduction. This increase was more pronounced for LptA than LptB, which would occur if LptA can bind to both the inner membrane complex and excess LptC in the membrane whereas LptB can only bind to the inner membrane complex (Fig. 2d). To test whether the number of bridges in the cell changed, we determined the normalized number of immobile tracks for LptA, LptB and LptC with LptC overexpression. We found an increase for LptA, a negligible change for LptB and no change for LptC (Fig. 2g). LptA must have an additional immobile state that is dependent on the overexpression of LptC, and this state is likely to be LptDE–A–C (Fig. 2d). By contrast, the sole source of immobile LptB is the full bridge state with all Lpt proteins present, with the absolute amount of the bridge remaining unchanged upon LptC overproduction. Therefore, the immobile state of LptB reports on the abundance of Lpt bridges in cells.

### Two distinct Lpt bridges are observed

We next examined the stabilities of the bridges by measuring lifetimes for the immobile states of LptA, LptB and LptC. Lifetime distribution plots for immobile LptA, LptB and LptC were remarkably similar, displaying an average lifetime of around 10 s (Fig. 3a). The nearly identical nature of the lifetime distributions implies that all three proteins report on the lifetime of the bridging state. We showed above that detectable LptA is largely bound to LptDE after the bridge breaks (Fig. 2). Therefore, it must be the case that LptDE-bound LptA can exchange rapidly with LptA from the pool of soluble unlabelled LptA–Halo in the periplasm. Thus, the signal from the LptDE-bound state declines rapidly under these conditions. For all three proteins, the lifetime data fit a biexponential decay reflecting two processes with half-lives of approximately 4 s and 12 s (Fig. 3b). The biexponential behaviour implies that two different states of the bridge can break. A plausible scenario is that in one state the bridge contains LPS whereas in the other LPS is absent.

We postulated that the presence of LPS in bridges could affect their properties by changing the number of bridges or their dynamics. We treated cells containing Halo–LptB with an LpxC inhibitor<sup>39</sup>, which decreases the intracellular LPS concentration by inhibiting the first

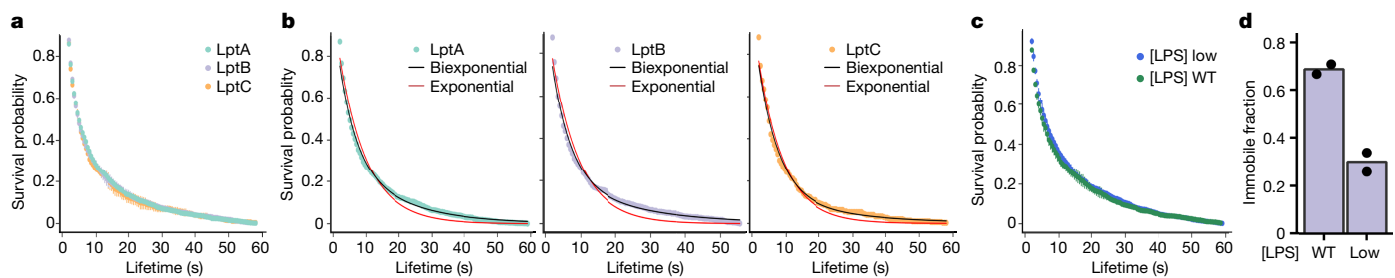


**Fig. 3 | Bridges break and form rapidly, with bridge formation facilitated by LPS.** **a**, Measured lifetimes for Halo-tagged LptA ( $n = 2,140$ ), LptB ( $n = 1,837$ ) and LptC ( $n = 708$ ) in the immobile state are shown in survival probability plots. Lifetimes were measured by fitting intensity traces of immobile spots to a hidden Markov model<sup>24</sup>. The average of two independent experiments is shown with standard deviations (error bars). **b**, Single exponential and biexponential curves are fitted to the lifetime plots of LptA, LptB and LptC. The line shows the fit to the model and dots show lifetime data. Plots are representative of two independent experiments. Residuals plots are presented in Extended Data Fig. 6 and fitted values can be found in Extended Data Fig. 7b. **c**, Lifetime distribution plots of immobile Halo-LptB tracks without (WT:  $n = 1,511$ ) and

with (low:  $n = 1,949$ ) LpxC inhibitor treatment (low; approximately  $0.5 \times$  minimum inhibitory concentration (MIC)). The average of two independent experiments is shown with standard deviations (error bars). **d**, The immobile fractions of single-molecule LptB tracks, measured without (WT) and with LpxC inhibitor treatment (low; approximately  $0.5 \times$  MIC). The bar depicts the average of two independent experiments. Independent experimental values are depicted as dots. WT:  $3,707/2$ ; low:  $n = 17,015/2$  (trajectories/independent experiments).  $\alpha$  is the immobile fraction obtained by the CDF fit. CDF fit results and samples sizes are reported in Supplementary Table 5. Corresponding confinement radius plots for the tracks can be found in Extended Data Fig. 7f.

committed step of LPS synthesis. Under the conditions used, there were no substantial changes in cell morphology (Extended Data Fig. 7e). However, the amount of LPS decreased by approximately 50% relative to untreated controls (Extended Data Fig. 7c). The lifetime distribution plot for immobile Halo-LptB was identical in the presence and absence of LpxC inhibitor, meaning that lowering the cellular concentration of LPS did not affect bridge breakage decay kinetics (Fig. 3c). However, the immobile fraction of Halo-LptB, which reports on the relative number of bridges, decreased substantially in the presence of LpxC inhibitor (Fig. 3d). There was a decrease in the amount of LptA in the presence of LpxC inhibitor that mirrored the decrease in LPS levels (Extended Data Fig. 7c). LptA is degraded when LpxC is inhibited<sup>40</sup>, suggesting that LPS depletion changes bridge stability. Because we observed that the rate of breaking bridges stayed the same, but the number of Lpt bridges in cells decreased, the rate of bridge formation must be lower when the LPS concentration decreases. Although we cannot exclude the possibility that indirect effects are responsible for changes in the relative number of bridges observed, a simple interpretation of our findings is that the presence of LPS lowers the barrier to bridge formation, leading to stabilization of LptA in the bridged state. If so, LPS is both a substrate for bridge transport as well as a structural component of the bridge. Because the bridge decay kinetics were not dependent on LPS concentration, the rate of dissociation of the structural LPS bound to the Lpt transporter must be slow relative to LPS transport. This model suggests that LPS binding to LptB<sub>2</sub>FGC in the inner membrane to form a complex containing a preloaded structural LPS lowers the barrier to connect to LptDEA.

### Bound LPS slows bridge disassembly

If the structural LPS in the inner membrane complex facilitates the LptC-LptA interaction for bridge formation, we explored whether this increased stability influences the rate of bridge breakage. We tested the effect of artificially stabilizing the LptC-LptA interface on bridge lifetimes by fusing LptC to LptA. This LptC-LptA (CA) fusion protein supports outer membrane assembly in cells lacking the individual proteins (S. Early et al., manuscript in preparation). When we monitored the immobile state of LptB to obtain bridge lifetimes in the presence of the CA fusion, we found that a single exponential now fit the observed decay (Fig. 4b), resulting in a half-life of approximately 8 s. The observation that the CA fusion exhibits a single exponential decay implies that fragmentation at the CA interface is one of the two

bridge breakage processes observed for the wild-type bridge. The other process must involve fragmentation at the LptD-LptA interface. Because fixing the bond between LptC and LptA results in a longer bridge lifetime (Fig. 4c), the faster cleavage process captured by the 4 s half-life for the wild-type bridge probably corresponds to dissociation at the LptC-LptA interface. We also examined effects on stability, and observed that the relative number of bridges for the CA fusion was lower than for the wild-type bridge under similar conditions, which implies that the rate of LptB<sub>2</sub>FGC-CA fusion bridge formation is slower than for the wild-type case, in which LptA preferentially associates with LptDE before associating with the inner membrane complex to form a bridge (Fig. 4d).

Together, our data suggest the following model for how bridges form and break in cells (Fig. 4e). In the unbridged state, LptB<sub>2</sub>FGC forms at the inner membrane, and soluble LptA preferentially associates at the outer membrane to form LptADE. When cells require more outer membrane, LPS biosynthesis produces an accumulation of LPS in the inner membrane, leading to an interaction with LptB<sub>2</sub>FGC to form LptB<sub>2</sub>FGC-LPS<sup>41</sup>. The preloaded inner membrane complex facilitates bridge formation with LptDEA to enable rapid transport of LPS to the outer membrane. There are two rates for breaking wild-type bridges that represent rupture at two different interfaces, because there are two different bridge states. The faster rate occurs for a state in which a structural LPS is not bound; in this case, breakage occurs at the LptC-LptA interface. The slower rate occurs for the state containing a structural LPS, which stabilizes the LptC-LptA interface such that breakage occurs at the otherwise more stable LptD-LptA interface.

In toto, we provide direct evidence that Lpt bridges exist in cells and characterize two bridge states having different lifetimes. Our methods did not allow us to determine the absolute number of bridges per cell. However, ribosome profiling performed under growth conditions similar to those used here has shown that there are approximately 250 copies of LptC, the limiting component of the Lpt pathway, in each *E. coli* cell<sup>42</sup>. Because we have found that at any given time half of the Lpt membrane proteins exist in a bridge state (Fig. 1g), we can therefore estimate that there are approximately 125 bridges per cell. Calculations suggest that around 2 million LPS molecules must be transported to the cell surface during each 30-min division cycle<sup>43</sup>. Each bridge must therefore transport approximately ten LPS molecules per second<sup>42,43</sup>. This rate agrees remarkably well with previously estimated values for LPS assembly on the cell surface<sup>28,44</sup>. If we assume that transport of one LPS molecule requires hydrolysis of one ATP, then the

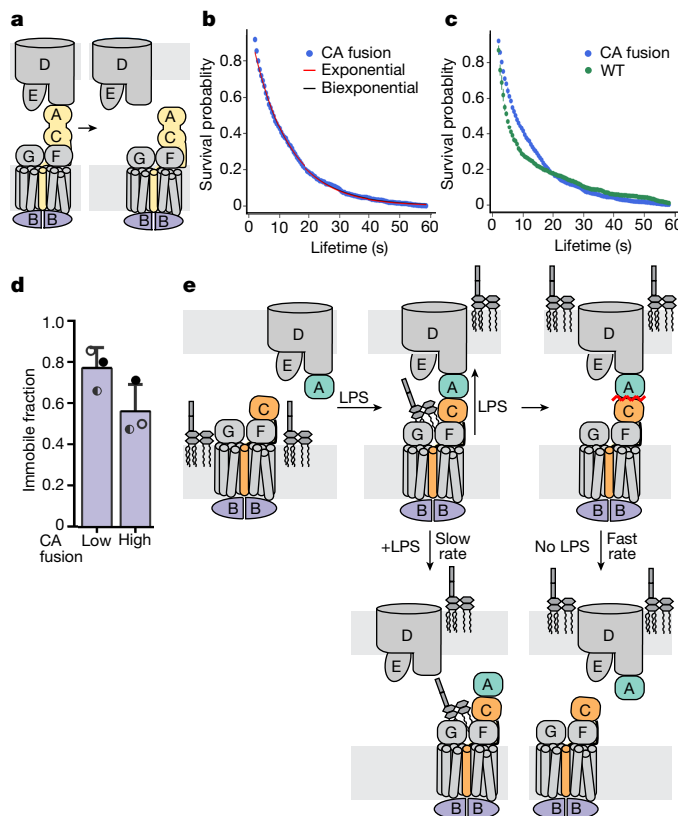


**Fig. 4 | Model for coordinating intermembrane Lpt bridge formation with LPS transport.** **a**, Schematic depicting Lpt bridge breakage when bridges contain the CA fusion protein. **b**, Single exponential and biexponential curves are fitted to the lifetime plot of LptB in the presence of the CA fusion protein. The lines show the fit and dots show the lifetime data. Fitted values and residual plots are presented in Extended Data Fig. 7b,h,i. A representative plot of two independent experiments is shown. **c**, Survival probability plots of LptB lifetimes with (CA:  $n=1,286$ ) and without (WT:  $n=1,047$ ) overproduction of the CA fusion protein. The average of two independent experiments is shown with standard deviations (error bars). **d**, Immobile fractions of single-molecule LptB tracks, measured without (low) or with (high) induction of CA fusion protein expression. The bar depicts the average of three independent experiments and dots show independent experimental values. Simultaneously performed experiments are denoted with the same dot type. LptC-LptA low:  $n=13,485/3$ ; LptC-LptA high:  $n=14,491/3$  (trajectories/independent experiments).  $\alpha$  is the immobile fraction obtained by the CDF fit. CDF fit results and sample sizes are reported in Supplementary Table 5. Corresponding confinement radius plot for the tracks can be found in Extended Data Fig. 7g. **e**, Schematic depicting a model for bridge formation and breakage.

required ATP hydrolysis rate of ten molecules per second is similar to that measured for the paradigmatic ATPase, ClpXP<sup>45</sup>. We have shown that Lpt bridges are short-lived (on the order of seconds); therefore, to meet transport needs during cell growth, LPS transport needs to be carefully coordinated with bridge formation. Our findings that LPS promotes bridge formation, and that its presence correlates with bridge stability, provide a mechanism to link LPS abundance to cell growth<sup>40</sup>.

## Online content

Any methods, additional references, Nature Portfolio reporting summaries, source data, extended data, supplementary information, acknowledgements, peer review information; details of author contributions and competing interests; and statements of data and code availability are available at <https://doi.org/10.1038/s41586-023-06709-x>.

- Osborn, M., Gander, J., Parisi, E. & Carson, J. Mechanism of assembly of the outer membrane of *Salmonella typhimurium*: isolation and characterization of cytoplasmic and outer membrane. *J. Biol. Chem.* **247**, 3962–3972 (1972).
- Kamio, Y. & Nikaido, H. Outer membrane of *Salmonella typhimurium*: accessibility of phospholipid head groups to phospholipase C and cyanogen bromide activated dextran in the external medium. *Biochemistry* **15**, 2561–2570 (1976).
- Mühlradt, P. F. & Golecki, J. R. Asymmetrical distribution and artifactual reorientation of lipopolysaccharide in the outer membrane bilayer of *Salmonella typhimurium*. *Eur. J. Biochem.* **51**, 343–352 (1975).
- Raetz, C. R. & Whitfield, C. Lipopolysaccharide endotoxins. *Annu. Rev. Biochem.* **71**, 635–700 (2002).
- Sperandeo, P. et al. Functional analysis of the protein machinery required for transport of lipopolysaccharide to the outer membrane of *Escherichia coli*. *J. Bacteriol.* **190**, 4460–4469 (2008).
- Chng, S.-S., Gronenberg, L. S. & Kahne, D. Proteins required for lipopolysaccharide assembly in *Escherichia coli* form a transenvelope complex. *Biochemistry* **49**, 4565–4567 (2010).
- Sherman, D. J. et al. Lipopolysaccharide is transported to the cell surface by a membrane-to-membrane protein bridge. *Science* **359**, 798–801 (2018).
- Sperandeo, P. et al. Characterization of lptA and lptB, two essential genes implicated in lipopolysaccharide transport to the outer membrane of *Escherichia coli*. *J. Bacteriol.* **189**, 244–253 (2007).
- Ruiz, N., Gronenberg, L. S., Kahne, D. & Silhavy, T. J. Identification of two inner-membrane proteins required for the transport of lipopolysaccharide to the outer membrane of *Escherichia coli*. *Proc. Natl Acad. Sci. USA* **105**, 5537–5542 (2008).
- Narita, S.-I. & Tokuda, H. Biochemical characterization of an ABC transporter LptBFGC complex required for the outer membrane sorting of lipopolysaccharides. *FEBS Lett.* **583**, 2160–2164 (2009).
- Sherman, D. J. et al. Decoupling catalytic activity from biological function of the ATPase that powers lipopolysaccharide transport. *Proc. Natl Acad. Sci. USA* **111**, 4982–4987 (2014).
- Owens, T. W. et al. Structural basis of unidirectional export of lipopolysaccharide to the cell surface. *Nature* **567**, 550–553 (2019).
- Li, Y., Orlando, B. J. & Liao, M. Structural basis of lipopolysaccharide extraction by the LptB-FGC complex. *Nature* **567**, 486–490 (2019).
- Suits, M. D., Sperandeo, P., Dehò, G., Polissi, A. & Jia, Z. Novel structure of the conserved Gram-negative lipopolysaccharide transport protein A and mutagenesis analysis. *J. Mol. Biol.* **380**, 476–488 (2008).
- Tran, A. X., Trent, M. S. & Whitfield, C. The LptA protein of *Escherichia coli* is a periplasmic lipid A-binding protein involved in the lipopolysaccharide export pathway. *J. Biol. Chem.* **283**, 20342–20349 (2008).
- Bos, M. P., Tefsen, B., Geurtzen, J. & Tommassen, J. Identification of an outer membrane protein required for the transport of lipopolysaccharide to the bacterial cell surface. *Proc. Natl Acad. Sci. USA* **101**, 9417–9422 (2004).
- Braun, M. & Silhavy, T. J. Imp/OstA is required for cell envelope biogenesis in *Escherichia coli*. *Mol. Microbiol.* **45**, 1289–1302 (2002).
- Wu, T. et al. Identification of a protein complex that assembles lipopolysaccharide in the outer membrane of *Escherichia coli*. *Proc. Natl Acad. Sci. USA* **103**, 11754–11759 (2006).
- Chng, S.-S., Ruiz, N., Chimalakonda, G., Silhavy, T. J. & Kahne, D. Characterization of the two-protein complex in *Escherichia coli* responsible for lipopolysaccharide assembly at the outer membrane. *Proc. Natl Acad. Sci. USA* **107**, 5363–5368 (2010).
- Freinkman, E., Chng, S.-S. & Kahne, D. The complex that inserts lipopolysaccharide into the bacterial outer membrane forms a two-protein plug-and-barrel. *Proc. Natl Acad. Sci. USA* **108**, 2486–2491 (2011).
- Cho, H. et al. Bacterial cell wall biogenesis is mediated by SEDS and PBP polymerase families functioning semi-autonomously. *Nat. Microbiol.* **1**, 16172 (2016).
- Bisson-Filho, A. W. et al. Treadmilling by FtsZ filaments drives peptidoglycan synthesis and bacterial cell division. *Science* **355**, 739–743 (2017).
- Garner, E. C. et al. Coupled, circumferential motions of the cell wall synthesis machinery and MreB filaments in *B. subtilis*. *Science* **333**, 222–225 (2011).
- Squires, G. R. et al. Single-molecule imaging reveals that Z-ring condensation is essential for cell division in *Bacillus subtilis*. *Nat. Microbiol.* **6**, 553–562 (2021).
- Lee, T. K., Meng, K., Shi, H. & Huang, K. C. Single-molecule imaging reveals modulation of cell wall synthesis dynamics in live bacterial cells. *Nat. Commun.* **7**, 13170 (2016).
- Rassam, P. et al. Intermembrane crosstalk drives inner-membrane protein organization in *Escherichia coli*. *Nat. Commun.* **9**, 1082 (2018).
- Mühlradt, P. F., Menzel, J., Golecki, J. R. & Speth, V. Lateral mobility and surface density of lipopolysaccharide in the outer membrane of *Salmonella typhimurium*. *Eur. J. Biochem.* **43**, 533–539 (1974).
- Mühlradt, P. F., Menzel, J., Golecki, J. R. & Speth, V. Outer membrane of *Salmonella*: sites of export of newly synthesised lipopolysaccharide on the bacterial surface. *Eur. J. Biochem.* **35**, 471–481 (1973).
- Rassam, P. et al. Supramolecular assemblies underpin turnover of outer membrane proteins in bacteria. *Nature* **523**, 333–336 (2015).
- Rojas, E. R. et al. The outer membrane is an essential load-bearing element in Gram-negative bacteria. *Nature* **559**, 617–621 (2018).
- Leake, M. C. et al. Stoichiometry and turnover in single, functioning membrane protein complexes. *Nature* **443**, 355–358 (2006).
- Oh, D., Yu, Y., Lee, H., Wanner, B. L. & Ritchie, K. Dynamics of the serine chemoreceptor in the *Escherichia coli* inner membrane: a high-speed single-molecule tracking study. *Biophys. J.* **106**, 145–153 (2014).
- Grimm, J. B. et al. A general method to improve fluorophores for live-cell and single-molecule microscopy. *Nat. Methods* **12**, 244–250 (2015).
- Lepore, A. et al. Quantification of very low-abundant proteins in bacteria using the HaloTag and epi-fluorescence microscopy. *Sci. Rep.* **9**, 7902 (2019).
- Mullineaux, C. W., Nenninger, A., Ray, N. & Robinson, C. Diffusion of green fluorescent protein in three cell environments in *Escherichia coli*. *J. Bacteriol.* **188**, 3442–3448 (2006).

36. Schütz, G. J., Schindler, H. & Schmidt, T. Single-molecule microscopy on model membranes reveals anomalous diffusion. *Biophys. J.* **73**, 1073–1080 (1997).
37. Sperandeo, P. et al. New insights into the Lpt machinery for lipopolysaccharide transport to the cell surface: LptA–LptC interaction and LptA stability as sensors of a properly assembled transenvelope complex. *J. Bacteriol.* **193**, 1042–1053 (2011).
38. Villa, R. et al. The *Escherichia coli* Lpt transenvelope protein complex for lipopolysaccharide export is assembled via conserved structurally homologous domains. *J. Bacteriol.* **195**, 1100–1108 (2013).
39. Montgomery, J. I. et al. Pyridone methylsulfone hydroxamate LpxC inhibitors for the treatment of serious Gram-negative infections. *J. Med. Chem.* **55**, 1662–1670 (2012).
40. Martorana, A. M. et al. Degradation of components of the Lpt transenvelope machinery reveals LPS-dependent Lpt complex stability in *Escherichia coli*. *Front. Mol. Biosci.* **8**, 758228 (2021).
41. Servais, C. et al. Lipopolysaccharide biosynthesis and traffic in the envelope of the pathogen *Brucella abortus*. *Nat. Commun.* **14**, 911 (2023).
42. Li, G.-W., Burkhardt, D., Gross, C. & Weissman, J. S. Quantifying absolute protein synthesis rates reveals principles underlying allocation of cellular resources. *Cell* **157**, 624–635 (2014).
43. Lima, S., Guo, M. S., Chaba, R., Gross, C. A. & Sauer, R. T. Dual molecular signals mediate the bacterial response to outer-membrane stress. *Science* **340**, 837–841 (2013).
44. Bishop, R. E. Lipopolysaccharide rolls out the barrel. *Nature* **511**, 37–38 (2014).
45. Kenniston, J. A., Baker, T. A., Fernandez, J. M. & Sauer, R. T. Linkage between ATP consumption and mechanical unfolding during the protein processing reactions of an AAA+ degradation machine. *Cell* **114**, 511–520 (2003).

**Publisher's note** Springer Nature remains neutral with regard to jurisdictional claims in published maps and institutional affiliations.

Springer Nature or its licensor (e.g. a society or other partner) holds exclusive rights to this article under a publishing agreement with the author(s) or other rightsholder(s); author self-archiving of the accepted manuscript version of this article is solely governed by the terms of such publishing agreement and applicable law.

© The Author(s), under exclusive licence to Springer Nature Limited 2023

# Article

## Methods

### Strain construction

Halo-Lpt strains were constructed by integrating Halo-Lpt fusion proteins at a phage attachment site<sup>46</sup>, while the wild-type chromosomal copy of the respective Lpt protein was knocked out. For LptD–Halo, the HaloTag was integrated at the native chromosomal site of LptD by lambda red recombineering. A list of strains used in this study is in Supplementary Table 1, a list of plasmids in Supplementary Table 2, and a list of primers is in Supplementary Table 3. HaloTag and linker sequences are given in Supplementary Table 4. The 15-amino-acid linker was used for tagging LptB, LptC and LptE. The 30-amino-acid linker was used for LptA and LptD.

### LT16 and LT138 for Halo–LptC expression

N-terminal Flag-tagged LptC has previously been shown to complement in cells lacking endogenous LptC<sup>46</sup>; we therefore added the HaloTag at the N terminus of LptC utilizing a 15-amino-acid linker between HaloTag and LptC. To create strains expressing Halo–LptC in place of endogenous LptC (LT16), pHc94C was electroporated into TB28 cells containing the temperature-sensitive helper plasmid pTB102. Colonies were selected on medium containing tetracycline. Single-copy integration of Plac::HaloTag::15-amino-acid linker::LptC at the phage attachment site attHK022 was confirmed by Sanger sequencing (Eton Bioscience). The resulting strain is LT138. To delete the native copy of LptC from the chromosome of LT138, the ΔLptC::frt::kan::frt allele<sup>6</sup> was transduced into the Halo–LptC strain using P1. Kanamycin-containing medium was used to select for transduction, and the successful deletion of the chromosomal LptC copy was confirmed by Sanger sequencing (Eton Bioscience). The kanamycin resistance allele was then switched out using the pCP20 plasmid, resulting in strain LT16.

### LT17 and LT137 for Halo–LptB expression

For LptB, C-terminal tags result in decreased function<sup>11</sup>, so we added the HaloTag to the N terminus, which has previously been shown to exhibit wild-type ATPase activity and growth when His-tagged<sup>47</sup>. LT17 was created analogously to LT16. In this case, pHc94B was electroporated into TB28 cells containing the temperature-sensitive pTB102 yielding LT137. The wild-type copy of LptB in the chromosome of LT137 was deleted by P1 transducing ΔLptB::frt::kan::frt cassette from strain NR2339<sup>11</sup>. The kanamycin resistance cassette was switched out with pCP20 to yield LT17.

### LT23 and LT136 for LptA–Halo expression

The N and C termini of LptA are important for its interactions with LptC and LptD, respectively. We tagged the C terminus, as this modification has previously been shown to support cell growth<sup>46</sup>. Additionally, between LptA and the HaloTag, we included a 30-amino-acid linker to enable interactions between the C terminus of LptA and the N terminus of LptD. LT23 was made analogously to LT16. Plasmid pHc94A was used to integrate Plac::LptA::30-amino-acid linker::HaloTag at the phage attachment site yielding LT136. To delete the wild-type chromosomal LptA in LT136, the ΔLptA::frt::kan::frt cassette was transduced from strain NR1849<sup>48</sup>. The kanamycin resistance marker was switched out with pCP20 to yield LT23.

### LT63 for Halo–LptE expression

To create N-terminally tagged Halo–LptE, we cloned its signal sequence and lipidation sequence upstream of the HaloTag to ensure correct secretion and lipidation. LT63 was created analogously to LT16. In this case, pHc94E was used to integrate Plac::LptE signal sequence–lipidation sequence + 6-amino-acid–HaloTag::15-amino-acid linker::LptE at the phage attachment site yielding LT61. The ΔLptE::frt::kan::frt cassette from strain MG1029<sup>49</sup> was P1 transduced to delete the wild-type

copy of LptE. The kanamycin resistance allele was switched out using pCP20 to yield LT63.

### LT18 for LptD–Halo expression

The N terminus of LptD interacts with LptA. Therefore, we added the Halo tag to the C terminus, which has previously been successfully tagged for purification purposes<sup>19</sup>. LT18 was constructed using lambda red recombineering. The frt::kan::frt cassette was amplified by PCR from pKD4 with primers LT185 and LT183, resulting in a PCR product that has a 50-bp overlap on its 3' end to the genome downstream of LptD. The DNA fragment 28-amino-acid linker::30-amino-acid linker::HaloTag was amplified by PCR from plasmid pBAD18–LptD–Halo with primers LT186 and LT178. The primers were chosen so that a 75 base pair overlap to LptD was created at the 5' end. The two PCR products were Gibson assembled to one fragment, overlap-LptD::28-amino-acid linker::30-amino-acid linker::HaloTag::frt::kan::frt::overlap-genome<sup>50</sup>. The Gibson product was amplified by PCR with primers LT178, LT184 and electroporated into MG1655 containing temperature-sensitive pKD46. Recombineering products were selected with medium containing kanamycin, and successful integration of a single 28-amino-acid linker::30-amino-acid linker::HaloTag::frt::kan::frt cassette into the correct chromosomal site was confirmed by Sanger sequencing. Following this, the kanamycin resistance allele was flipped out using pCP20.

### Plasmid construction

**pHC94A.** gLptA was amplified by PCR from the MG1655 genome using primers LT41 and LT42. The 30-amino-acid linker::HaloTag fragment was amplified by PCR using primers LT44 and LT9. The two fragments were assembled using Gibson Assembly Master mix. The resulting LptA::30-amino-acid linker–HaloTag fragment was amplified by PCR with primers LT214 and LT215 and digested with XbaI and HindIII. Plasmid pHc943 was digested with XbaI and HindIII, and the two digested products were ligated to form pHc94A. The ligated product was transformed into DH5α(λpir) cells.

**pHC94B.** A HaloTag::15-amino-acid linker::LptB fragments was generated by PCR amplifying genomic DNA of LptB (MG1655) with LT78, LT93, amplifying HaloTag::15-amino-acid linker with LT2, LT81, and Gibson assembling both fragments. HaloTag::15-amino-acid linker::LptB was amplified by PCR with LT208, LT209 digested with XbaI and HindIII and ligated into XbaI and HindIII-digested pHc943. The ligated product was transformed into DH5α(λpir) cells.

**pHC94C.** HaloTag::15-amino-acid linker::LptC was generated by PCR amplifying genomic LptC of MG1655 with LT11, LT26, and HaloTag::15-amino-acid linker with LT27, LT67 and assembling these two fragments using Gibson assembly master mix. The resulting DNA fragment was amplified by PCR with LT211 and LT210, digested with XbaI and HindIII, and ligated into digested pHc943 to form pHc94C. The ligated product was transformed into DH5α(λpir) cells.

**pHC94E.** To ensure secretion and lipidation of Halo–LptE, the signal sequence and the first seven amino acids (CGWHCRD) of LptE were added in front of the HaloTag. After the 15-amino-acid linker, LptE starts with CGWHCRD again. The complete sequence for the Halo–LptE is given in Supplementary Table 4. Three DNA segments were amplified by PCR: LptE signal sequence–lipidation sequence + 6 amino acids (genomic signal sequence from LptE plus the first 7 amino acids of LptE) with LT204, LT202, HaloTag::15-amino-acid linker with LT203, LT206, and genomic LptE from MG1655 with LT205, LT207. The three fragments were assembled using Gibson assembly method to ssLptE::HaloTag::15-amino-acid linker::LptE. The resulting fragment was amplified by PCR with LT212 and LT213, digested with XbaI and HindIII, and ligated into XbaI and HindIII-digested pHc943. The ligated product was transformed into DH5α(λpir) cells.

**pBAD33-LptC.** gLptC from MG1655 was amplified by PCR from the genome with LT247, LT26, and pBAD33 was amplified by PCR with LT273, LT274. To generate pBAD33-LptC, the two fragments were assembled using Gibson assembly. The assembled product was transformed into NovaBlue cells.

**pBAD33-LptC(G153R).** pBAD33-LptC(G153R) was generated using site-directed mutagenesis. For this, pBAD33-LptC was amplified by PCR with primer LT271 and LT272. The product was DpnI digested and transformed into NovaBlue cells.

**pBAD18LptD-Halo.** To create pBAD18-LptD-Halo, LptD plus the 28-amino-acid linker were amplified by PCR from pET23/42LptD plasmid<sup>19</sup> with primers LT37, LT188. The 30-amino-acid linker::HaloTag was amplified by PCR with LT187, LT9, and pBAD18 was amplified with primers LT46, LT40. All three PCR products were Gibson assembled and the resulting product transformed. Pbad18LptD-Halo expresses LptD–HaloTag fusion in which the HaloTag is fused to LptD with two linkers.

**pBAD33LptCA fusion.** The CA fusion protein was amplified using primers LT247 and LT314 from pBAD18LptC-(Gly-Gly-Gly-Gly-Ser)<sub>3</sub>-LptA-His (S. Early, A. Wilson, N. Ruiz, D. Kahne, manuscript in preparation). pBAD33 was amplified using primers LT316 and LT319. The two fragments were Gibson assembled and transformed into NovaBlue cells.

### Culture growth

Unless otherwise indicated, all cultures in this study were grown as described in the following procedure: cells were streaked from frozen stocks on LB agar plates and incubated overnight at 37 °C. Single colonies from the plates were inoculated in M9 medium, supplemented with 0.2% casamino acid (CAA) and 0.4% maltose as the carbon source, serially diluted, and grown overnight at 37 °C. The next day a culture at its mid-exponential phase ( $OD_{600} = 0.3\text{--}0.6$ ) was used as a starter culture to produce another round of serial dilutions. These were grown on the shaker at 37 °C until they reached  $OD_{600}$  of about 0.3. At this point, the strains were either stained and imaged or collected for immunoblotting.

To grow strains, expression of the respective Lpt–Halo fusion protein was induced by adding 20 μM IPTG for LT17, LT63, LT23, LT136, LT137 and LT61, and 70 μM IPTG for LT16 and LT138 to the medium.

### Immunoblots

For immunoblots, cultures were grown as described above to  $OD_{600}$  of about 0.3–0.4 and normalized to  $OD_{600}$  of about 10 for Extended Data Figs. 1a–e and 5a and to  $OD_{600}$  of about 0.3 for Extended Data Fig. 5b. The cells were pelleted with centrifugation at 12,000*g* for 5 min. The pellets were resuspended in 1× SDS–PAGE sample buffer supplemented with 5% β-mercaptoethanol except when noted otherwise for LptD samples. Samples were boiled for 10 min and run on homemade Tris-HCl 4–20% polyacrylamide gels. Proteins were transferred onto Immuno-Blot PVDF membranes (Bio-Rad). The membrane was blocked with 1× casein blocking buffer and then incubated with the primary antibody overnight. The sources of primary rabbit anti-LptC (1:2,000)<sup>40</sup>, LptA (1:10,000)<sup>40</sup>, LptB (1:10,000)<sup>11</sup>, LptE (1:10,000)<sup>6</sup>, and LptD (1:10,000)<sup>6</sup> antisera have been previously reported. Lpt proteins and BamA were detected by a donkey anti-rabbit HRP conjugated secondary antibody (1:10,000, GE Amersham, NA9340V). Anti-RpoA (1:2,000, BioLegends, 663104) and anti-HaloTag were detected with sheep anti-mouse HRP conjugated secondary antibody (1:10,000, ECL, NA931V). Bands were visualized using ECL Prime Western Blotting Detection Reagent (GE Amersham) and Azure c400 imaging system (Azure Biosystems).

### Growth curves

Single colonies of the strains were inoculated from streaked plates in M9 medium containing 0.2% casamino acid and 0.4% maltose. For

LT17/LT63/LT23, 20 μM IPTG, and for LT16, 70 μM IPTG was added to the medium to induce expression of the Lpt–HaloTag proteins. For LT18 and TB28, no inducer was added. The cultures were grown overnight at 37 °C and then diluted 1:100 into fresh medium the next morning. At  $OD_{600}$  of about 0.3, the cultures were diluted 1:1,000 into fresh medium in a 96-well plate. The diluted cultures were grown at 37 °C while shaking, and  $OD_{600}$  was monitored using a Tecan Magellan plate reader every 10 min for 12 h.

### Slide preparation

To reduce background fluorescence, the coverslips were cleaned before their use for total internal reflection fluorescence microscopy (TIRFM). The coverslips were sonicated for 30 min in 2% Hellmanex III, washed with deionized water, and subsequently sonicated in NaOH for 30 min. The NaOH was washed away with deionized water, and the coverslips were washed with ethanol and sonicated in ethanol for another 30 min. Coverslips were washed with ethanol again and stored in ethanol until their usage.

### Imaging sample preparation

Cultures of the strains were grown as described above. At  $OD_{600}$  of about 0.3, 1 ml of the culture was stained with approximately 5 nM *Janelia* Fluor HaloTag 549<sup>34</sup> and incubated for 10–15 min at 37 °C while shaking. The culture was concentrated by spinning it down at 8,000 rpm for 2 min and removing part of the supernatant. 1 μl of the concentrated culture was pipetted onto a 20 × 60 mm coverslip and covered with a 1.5 mm thick 2% agar pad. The agar pad was made with the medium in which the strain was grown in. After about 30 min of imaging, a new slide was prepared.

### Microscope setup for particle tracking

Total internal reflection fluorescence microscopy (TIRFM) and phase-contrast microscopy were performed on a Nikon TI microscope equipped with a 100× NA 1.45 TIRFM objective and an Andor Ixon EMCCD camera resulting in 160 nm pixels. NIS-Elements Microscope Imaging Software (version 5.02.01) was used to collect images. With an exposure time of 100 ms, 400–500 frames (streaming acquisition) were taken using an illumination of 561 nm. A phase-contrast image was taken before and after the fluorescent video was acquired to segment the outside of the cells. Videos that displayed drift were discarded. The imaging was performed in a chamber equilibrated at 37 °C.

### Immobilized dye measurement

Imaging slides were prepared as described above. Instead of applying cell solution to the slide, 0.5 μl of 12.5 μM *Janelia* Fluor HaloTag 549 dye solution was applied. An agarose pad was added above, and the sample was imaged as described above.

### Image analysis

Collected images were not modified for analysis. Images were analysed with Fiji<sup>51</sup>. For display purposes, images were cropped for the figures and videos.

### Particle tracking

Tracks were generated using the software Fiji and the plugin Track-Mate<sup>52</sup>. Particles were detected with the difference of Gaussian detector with subpixel localization, and tracks were generated using the simple LAP tracker with a 200 nm search radius and no frame gaps allowed. Tracks shorter than four frames were discarded, and the remaining tracks were exported for further processing.

### Data analysis

Unless otherwise indicated, further data analysis was done in Python using custom code. Plots were generated using Python Matplotlib or Graphpad PRISM.

## Filtering tracks in cells

To ensure only tracks inside cells are used for analysis, the phase-contrast images to the corresponding videos were converted into binary images using the threshold tool in Fiji. The exported binary images were used as a mask to filter out tracks from the exported TrackMate file which are not in cells. A custom Python code was used for this.

## MSD analysis

Mean squared displacements (MSD) versus time delay ( $\Delta t$ ) plots were generated for all tracked proteins. MSD versus  $\Delta t$  plots are shown for 20 representative tracks for each imaged protein in Extended Data Fig. 3. As tracks indicated switching behaviour between different dynamic states, we used confinement radius calculation and CDF analysis for further analysis.

## Confinement radius

For the confinement radius analysis, tracks were filtered to a minimum length of 5 frames. Tracks larger than 5 frames were cut down to 5 consecutive frames. The confinement radius was calculated by determining the average  $xy$  position (centroid) of the trajectory by averaging the trajectory coordinates. The average of the distances between the trajectories coordinates to the centroid gives the confinement radius. Confinement radii histograms were generated using the NumPy.histogram function<sup>53</sup> with a given bin size of 0.01. The histogram values were normalized by dividing the incident number per bin by the total number of incidences. The plots were generated using Matplotlib.

## Cumulative distribution function analysis

Trajectories were filtered to a minimum length of 4 frames and a maximum length of 150 frames. The  $r^2$  displacement was calculated for trajectories by measuring the frame-to-frame vector displacement along the trajectory by the lag time  $\Delta t = 200$  ms and taking its magnitude. The cumulative probability of displacement  $r$  in the observation period  $\Delta t$  ( $P(r^2, \Delta t)$ ) was constructed from the pool of displacements across multiple tracks for each protein by counting the number of squared displacements  $\leq r^2$  normalized by the sample size. The CDF of the  $r^2$  displacements was fitted to analytical functions describing diffusive processes with one or two dynamic states, ES1 and ES2<sup>36,54</sup>.  $D_1$  and  $D_2$  are diffusion constants for the different states, and  $\alpha$  describes the relative fraction between the states. The error term is  $4\sigma^2$ , with  $\sigma = 0.034$   $\mu\text{m}$ .  $\sigma$  was identified as the average of the confinement radii of immobilized dye tracks with a frame length of 3, and given for the fit as a fixed parameter. CDF fit results with  $\sigma = 0.034$   $\mu\text{m}$ , with a smaller error term, and without an error term are reported in Supplementary Table 5.

$$(ES1)P(r^2, \Delta t) = 1 - e^{-\frac{r^2}{4D_1\Delta t + 4\sigma^2}}$$

$$(ES2)P(r^2, \Delta t) = 1 - \left( \alpha \times e^{-\frac{r^2}{4D_1\Delta t + 4\sigma^2}} + (1 - \alpha) \times e^{-\frac{r^2}{4D_2\Delta t + 4\sigma^2}} \right)$$

The CDF for LptA, LptB and LptC under wild-type conditions were fitted with both different diffusion models using the lmfit package in Python<sup>55</sup>. Residuals of model fits were calculated and used to identify the best model. The two-component diffusive model resulted in the best fit for all three proteins. To identify the diffusion constant and the fraction of proteins in the immobile state for the proteins under non-wild-type conditions, only the two-state diffusive model was used. CDF fit results are reported in Supplementary Table 5.  $P$  values shown in Figs. 2c,e were obtained by an independent two-sided  $t$ -test using scipy.stats (version 1.2.3) package.

## Tracks per cell surface calculation

Cell masks were constructed as binary images, as explained above. The cell surface area was calculated by taking the sum of the binary image. Tracks were filtered to have a minimum length of 4 frames, a maximum length of 150 frames and to be inside cells. The number of tracks measured for one 400-frame time-lapse video was calculated and divided by the corresponding cell surface area. At least three time-lapse videos with their corresponding phase images were used to determine the tracks per cell surface. The values measured for tracks per cell surface and immobile tracks per cell surface for each condition and each time-lapse video are given in Supplementary Table 6.

To determine the immobile tracks per cell surface, tracks were additionally filtered for a confinement radius  $< 0.07$   $\mu\text{m}$  before the number of tracks is calculated.

## Lifetime measurement

For the lifetime measurements, strains were grown and imaging samples were prepared as described above. TIRFM time-lapse videos were taken with streaming 500-ms exposures for 4 min using the EMCCD camera at 561 nm illumination. A phase-contrast image was taken before and after each time-lapse, and a cell mask was generated using the threshold tool in Fiji. The analysis used for determining single-molecule lifetime was described and developed in<sup>24</sup>. The TIRFM time-lapses were preliminarily analysed using TrackMate. Spots were detected with the DoG detector and linked with a two-pixel linking distance and a maximum gap of ten frames. The TrackMate data were exported to Matlab.

To determine lifetimes from the TrackMate data, the Matlab code published and developed by G. Squyres was used<sup>56</sup>. The tracks from TrackMate were filtered for tracks inside cells using the generated cell masks, and the filtered tracks were converted into spot intensity traces. A  $5 \times 5$ -pixel window around the mean spot position was used to calculate the average intensity, and the local background was averaged in a 2-pixel frame around the window. The resulting intensity traces were filtered; only traces with a maximum background-subtracted intensity above 300 counts were included for further analysis. Intensity traces were fitted to a hidden Markov model using the vbFRET package<sup>57</sup> to measure single-molecule lifetimes. Only traces that were best fitted with a two-state model were included. Further, a minimum difference between state 1 (no fluorescence) and state 2 (single-molecule fluorescence) of 40 counts (50 counts for LpxC inhibitor data and its control) was set. The lifetime is given by the duration of each state 2 event: dwell times less than 2 s (four frames) were excluded, as well as events that overlapped with the start or the end of the trace. Traces with more than four events (three events for LpxC inhibitor data and its control) were also discarded. Treatment of cells with LpxC inhibitor resulted in higher background images. Therefore, more stringent lifetime analysis parameters were used for these data and the corresponding control.

The resulting lifetimes were exported as NumPy files<sup>53</sup> and further analysed with custom written Python code. Single-molecule lifetimes were plotted as survival probability by dividing the number of lifetimes  $>i$  by the total number of measured lifetimes, whereby  $i$  is equal to the minimum to maximum measured lifetimes in 500-ms steps. The single and the biexponential fits to the lifetime plots were done using the lmfit package in Python<sup>5</sup>.

To measure the contribution of photobleaching to the lifetime measurement, we repeated the lifetime measurement for Halo-LptC with 1-s imaging intervals rather than 500-ms intervals without changing the laser intensity or exposure time. There was no notable difference between the 1-s imaging intervals measurements compared to the 500-ms intervals, indicating that photobleaching contribution was negligible (Extended Data Fig. 7a).

## Cell length and width measurement

Cell length and width was measured manually in phase images using Fiji<sup>51</sup>. Randomly picked cells were measured for length by drawing a line between the two cell poles and measuring the line length using the ROI (region of interest tool). To measure the cell width, the line was drawn in the mid-cell region.

## Overproduction of mutants and drug treatment

**Imaging of strains with LptC(G153R) or wild-type LptC.** pBAD33-LptC(G153R) or wild-type LptC was transformed into LT16, LT17 and LT23. The strains containing the plasmid were grown as described above with the addition of chloramphenicol to the medium to ensure the retention of the plasmid. Imaging samples were prepared analogously to the description above. However, 10 min before staining, 40 mM arabinose was added to the culture to induce the production of LptC(G153R) or LptC. Agarose pads were prepared with medium containing chloramphenicol and arabinose. For the negative condition no arabinose was added. Data collected with the addition of 40 mM arabinose is indicated as 'high', and data collected without the addition of arabinose is marked with 'low' in Fig. 2. Videos for particle tracking were taken about 35 min after inducing the expression of LptC(G153R) or LptC with the same setup as defined above. For the concentration gradient (Fig. 2) arabinose concentrations of 0, 1 mM, 7 mM, 20 mM and 40 mM were used.

**LpxC inhibitor treatment.** Cultures of LT17 were grown as described above. Ninety minutes before staining the cells were treated with 0.24 μM LpxC inhibitor (PF 5081090)<sup>39</sup> (about 0.5× MIC). Also, the agarose pad to fix the cells to the microscope slides was prepared with 0.24 μM LpxC inhibitor. Since the outer membrane of cells treated with LpxC inhibitor becomes leaky, the labelling dye concentration was reduced to approximately 12.5 pM. Videos for particle tracking and lifetime measurement were collected as described above. For the negative control, LT17 was imaged without the addition of the LpxC inhibitor and with the usual dye concentration of approximately 5 nM. For the spot dilutions shown in Extended Data Fig. 7, cultures were diluted 90 min after LpxC inhibitor treatment 1:10 in PBS, serial diluted up to 10<sup>-6</sup> and 10 μl of the dilutions were pipetted onto LB agar and grown overnight at 37 °C.

**Silver stain.** LT17 starter cultures were grown as described in 'Culture growth'. After overnight growth, a mid-log culture was diluted 1:100 and grown at 37 °C until OD<sub>600</sub> of about 0.2–0.3, at which point cells were split and either untreated or treated with 0.24 μM LpxC inhibitor for 90 min. Cells were pelleted at 12,000g for 5 min, resuspended to an OD<sub>600</sub> of 20 in 1× LDS buffer (Invitrogen NP0007) + 4% β-mercaptoethanol, and boiled at 95 °C for 5–10 min. From these samples, the protein concentration was determined with G Biosciences NI Protein Assay (786-005). A volume equivalent of 20 μg of protein was loaded for immunoblots and run on homemade Tris-HCl 4–20% polyacrylamide gels. Immunoblots were stained and detected as described in the Immunoblots section above. A 50 μl aliquot was removed for proteinase K digestion (1.25 μl proteinase K, NEB) and silver stain; a volume equivalent of 2 μg of protein was loaded on 4–12% gels (Bio-Rad 3450124) for silver stain, and the silver staining protocol was performed as described<sup>58</sup>. The gel was imaged with the Azure c400 imaging system.

**Imaging of Halo-LptB with CA fusion.** pBAD33CA fusion was transformed into LT17. The strain containing the CA fusion plasmids was grown as described above with the addition of chloramphenicol to retain the plasmid. Ten minutes before staining the cultures, 40 mM arabinose was added to induce the production of the CA fusion protein. Arabinose and chloramphenicol were also added to the agarose pad. For the negative wild-type control, no arabinose was added to the

culture or the pad. Particle tracking and lifetime measurements were conducted as described above.

**Fractionation of LT23.** The fractionation of LT23 was done following the protocol used in<sup>6</sup>. In total, 1.5 L cells were grown of LT23 in LB at 37 °C to OD<sub>600</sub> of about 1.2. Cells were pelleted by centrifugation at 4,251g for 20 min and then resuspended in 15 ml of 10 mM Tris-HCl, pH 8.0 containing 20% (w/w) sucrose, 1 mM PMSF, and 50 μg ml<sup>-1</sup> DNase I. The cells were lysed by a single passage through the cell disruptor. Unbroken cells were removed by centrifugation at 3,000g for 20 min. A 1.6 ml volume of cell lysate was layered on top of the sucrose gradient: bottom 65% (0.5 ml), 55% (1.0 ml), 50% (2.4 ml), 45% (2.4 ml), 40% (2.4 ml), 35% (1.4 ml) and 30% (0.5 ml). All sucrose (w/w) solutions contained 10 M Tris-HCl, pH 8.0. Samples were centrifuged at 39,000 rpm for 15 h, and 0.5 ml fractions were collected manually from the top of each tube. Fractions were diluted with 950 μl of 20 mM Tris-HCl, pH 8.0 and 110 μl 100% (w/w) trichloroacetic acid (TCA, Sigma). Precipitated proteins were collected by centrifugation at 21,000g for 30 min, resuspended, and analysed by SDS-PAGE and immunoblotting. For sucrose fractionation immunoblots, LptA–Halo was detected with anti-HaloTag (1:1,000, Promega G921A), anti-LptF (1:20,000)<sup>38</sup> was run as a reference for inner membrane proteins, and anti-BamA (1:5,000)<sup>59</sup> blot was run as a reference for the outer membrane (Extended Data Fig. 5e).

**Figure production.** Figures shown in this paper were produced using INKSCAPE 1.2.1.

## Reporting summary

Further information on research design is available in the Nature Portfolio Reporting Summary linked to this article.

## Data availability

The data supporting the findings of the study are available in this article and its Supplementary Information files. Raw images and trajectory files are available at [https://dataverse.harvard.edu/dataverse/Lpt\\_tracking\\_data](https://dataverse.harvard.edu/dataverse/Lpt_tracking_data).

## Code availability

Code used in this paper is available at <https://github.com/Itoerk/Lpt-tracking-code>, and lifetime analysis code available at <https://bitbucket.org/garnerlab/squres-2020/src/master/Lifetime%20Analysis/>.

46. Haldimann, A. & Wanner, B. L. Conditional-replication, integration, excision, and retrieval plasmid-host systems for gene structure-function studies of bacteria. *J. Bacteriol.* **183**, 6384–6393 (2001).
47. Simpson, B. W. et al. Combining mutations that inhibit two distinct steps of the ATP hydrolysis cycle restores wild-type function in the lipopolysaccharide transporter and shows that ATP binding triggers transport. *mBio* **10**, e01931–01919 (2019).
48. Freinkman, E., Okuda, S., Ruiz, N. & Kahne, D. Regulated assembly of the transenvelope protein complex required for lipopolysaccharide export. *Biochemistry* **51**, 4800–4806 (2012).
49. Malojčić, G. et al. LptE binds to and alters the physical state of LPS to catalyze its assembly at the cell surface. *Proc. Natl Acad. Sci. USA* **111**, 9467–9472 (2014).
50. Gibson, D. G. et al. Enzymatic assembly of DNA molecules up to several hundred kilobases. *Nat. Methods* **6**, 343–345 (2009).
51. Schindelin, J. et al. Fiji: an open-source platform for biological-image analysis. *Nat. Methods* **9**, 676–682 (2012).
52. Ershov, D. et al. Bringing TrackMate in the era of machine-learning and deep-learning. Preprint at *bioRxiv* <https://doi.org/10.1101/2021.09.03.458852> (2021).
53. Harris, C. R. et al. Array programming with NumPy. *Nature* **585**, 357–362 (2020).
54. Bosch, P. J., Kanger, J. S. & Subramanian, V. Classification of dynamical diffusion states in single molecule tracking microscopy. *Biophys. J.* **107**, 588–598 (2014).
55. Newville, M. et al. LMFit: non-linear least-square minimization and curve-fitting for Python. Zenodo, <https://zenodo.org/records/11813> (2014).
56. Squires, G. R. Lifetime analysis <https://bitbucket.org/garnerlab/squres-2020/src/master/Lifetime%20Analysis/> (2020).
57. Bronson, J. E., Fei, J., Hofman, J. M., Gonzalez, R. L. Jr & Wiggins, C. H. Learning rates and states from biophysical time series: a Bayesian approach to model selection and single-molecule FRET data. *Biophys. J.* **97**, 3196–3205 (2009).

# Article

58. Fivenson, E. M. et al. A role for the Gram-negative outer membrane in bacterial shape determination. *Proc. Natl Acad. Sci. USA* **120**, e2301987120 (2023).
59. Kim, S. et al. Structure and function of an essential component of the outer membrane protein assembly machine. *Science* **317**, 961–964 (2007).

**Acknowledgements** The authors thank G. Squyres, M. Holmes and E. Fivenson for experimental advice; A. Polissi for the gift of the anti-LptA and anti-LptC antibodies; and T. Mitchison for providing feedback on the manuscript. This work was supported by NIH Grant R01 AI149778 and R01 AI081059 to D.K. Further, this work was funded by AI083365 from the NIH (National Institute for Allergy and Infectious Disease) and Investigator funds from the Howard Hughes Medical Institute to T.G.B.

**Author contributions** L.T. designed, performed and analysed experiments (all TIRFM experiments and data analyses, strain constructions, sucrose gradient fractionation and related immunoblots, growth curves, spot plate assay and LptC overexpression immunoblots), interpreted results and wrote the manuscript. C.B.M. performed experiments (silver stain and

related immunoblots, Lpt-HaloTag fusion immunoblots and LptC(G153R) immunoblots) and contributed to writing the revised manuscript. E.C.G. provided expertise in the design of the single-molecule tracking experiments. T.G.B. provided expertise in the design of genetic tools for constructing the fusion strains. D.K. designed experiments, interpreted results and wrote the manuscript. All authors contributed to editing.

**Competing interests** The authors declare no competing interests.

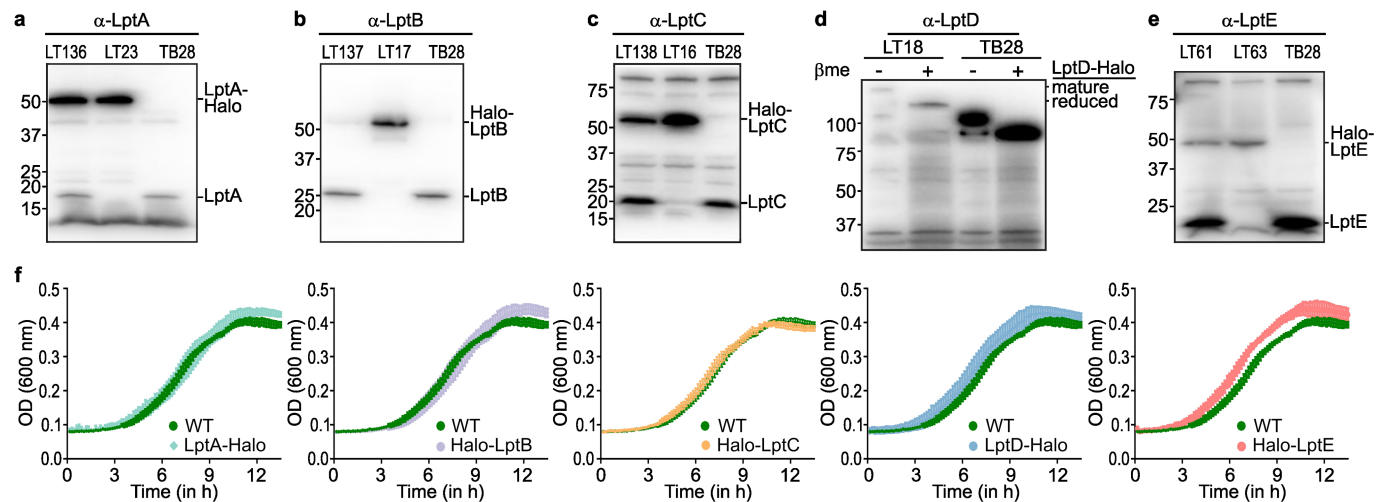
#### Additional information

**Supplementary information** The online version contains supplementary material available at <https://doi.org/10.1038/s41586-023-06709-x>.

**Correspondence and requests for materials** should be addressed to Ethan C. Garner or Daniel Kahne.

**Peer review information** *Nature* thanks Russell Bishop, Carol Gross and the other, anonymous, reviewer(s) for their contribution to the peer review of this work. Peer review reports are available.

**Reprints and permissions information** is available at <http://www.nature.com/reprints>.



### Extended Data Fig. 1 | Lpt-HaloTag fusions are expressed and support cell growth.

**a**,  $\alpha$ -LptA immunoblot of LT136 (expresses wild-type endogenous LptA (~20 kDa) and LptA-Halo (~53 kDa)), LT23 (expresses LptA-Halo) and TB28 (expresses wild-type endogenous LptA).

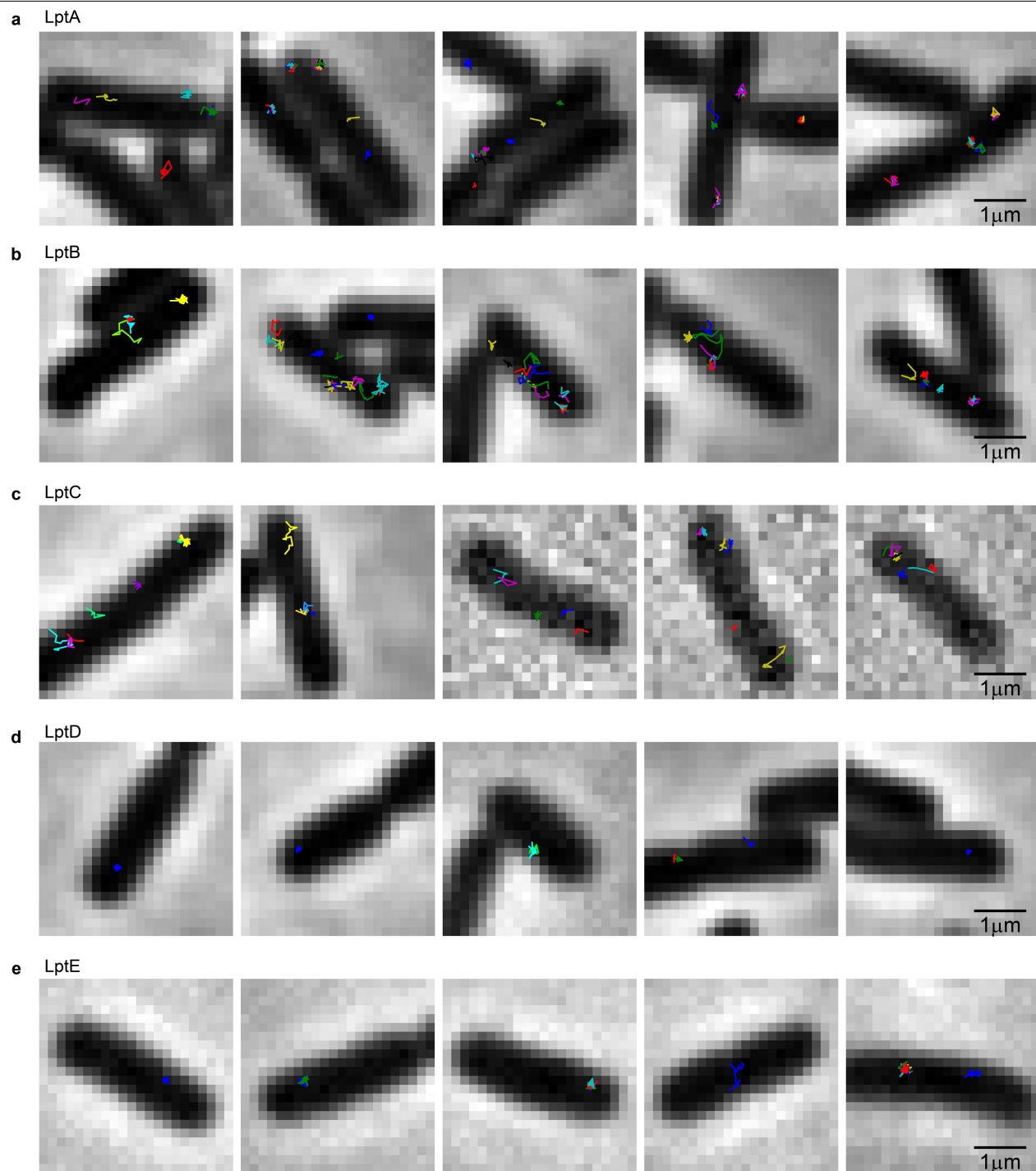
**b**,  $\alpha$ -LptB immunoblot of LT137 (expresses wild-type endogenous LptB (~25 kDa) and Halo-LptB (~55 kDa)), LT17 (expresses Halo-LptB), and TB28 (expresses wild-type endogenous LptB).

**c**,  $\alpha$ -LptC immunoblot of LT138 (expresses wild-type endogenous LptC (~20 kDa) and Halo-LptC (~55 kDa)), LT16 (expresses Halo-LptC) and TB28 (expresses wild-type endogenous LptC).

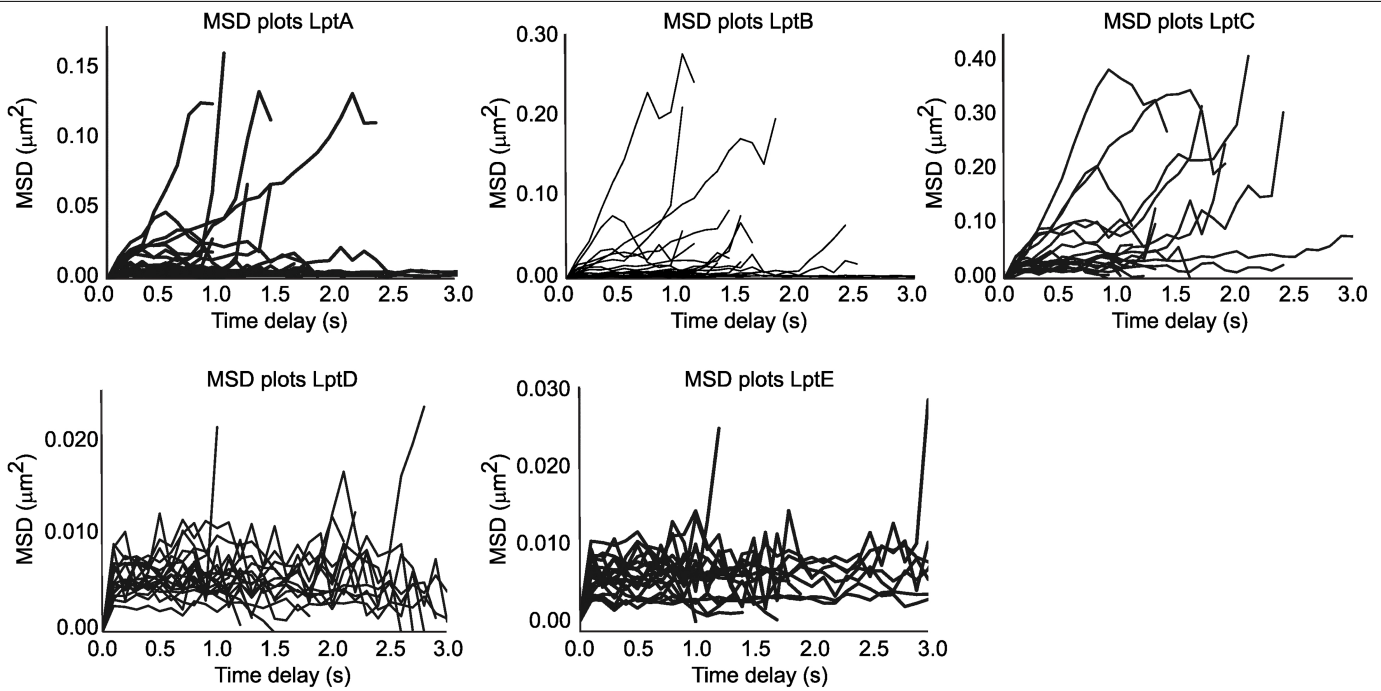
**d**,  $\alpha$ -LptD immunoblot of LT18 (expresses LptD-Halo) and TB28 (expresses wild-type endogenous LptD) without and with beta-mercaptoethanol ( $\beta$ me) treatment. Under nonreducing conditions, wild-type endogenous LptD is ~110 kDa and LptD-Halo is ~150 kDa.

The addition of  $\beta$ me reduces disulfide bonds in LptD and causes wild-type endogenous LptD to run around 87 kDa, and LptD-Halo to run around 120 kDa. LptD-Halo shows the same response to  $\beta$ me addition as wild-type LptD, confirming that it can properly fold<sup>19</sup>. **e**,  $\alpha$ -LptE immunoblot of LT61 (expresses wild-type endogenous LptE (~20 kDa) and Halo-LptE (~55 kDa)), LT63 (expresses Halo-LptE) and TB28 (expresses wild-type endogenous LptE). **a-e**, Shown results are representative of two independent experiments. LT136, LT137, LT138, and LT61 were included in blots as controls to identify bands. Uncropped gel images can be found in Supplementary Fig. 1. **f**, Growth curves of LT23 (LptA-Halo), LT17 (Halo-LptB), LT16 (Halo-LptC), LT18 (LptD-Halo), LT63 (Halo-LptE) and TB28 (WT, green).

# Article



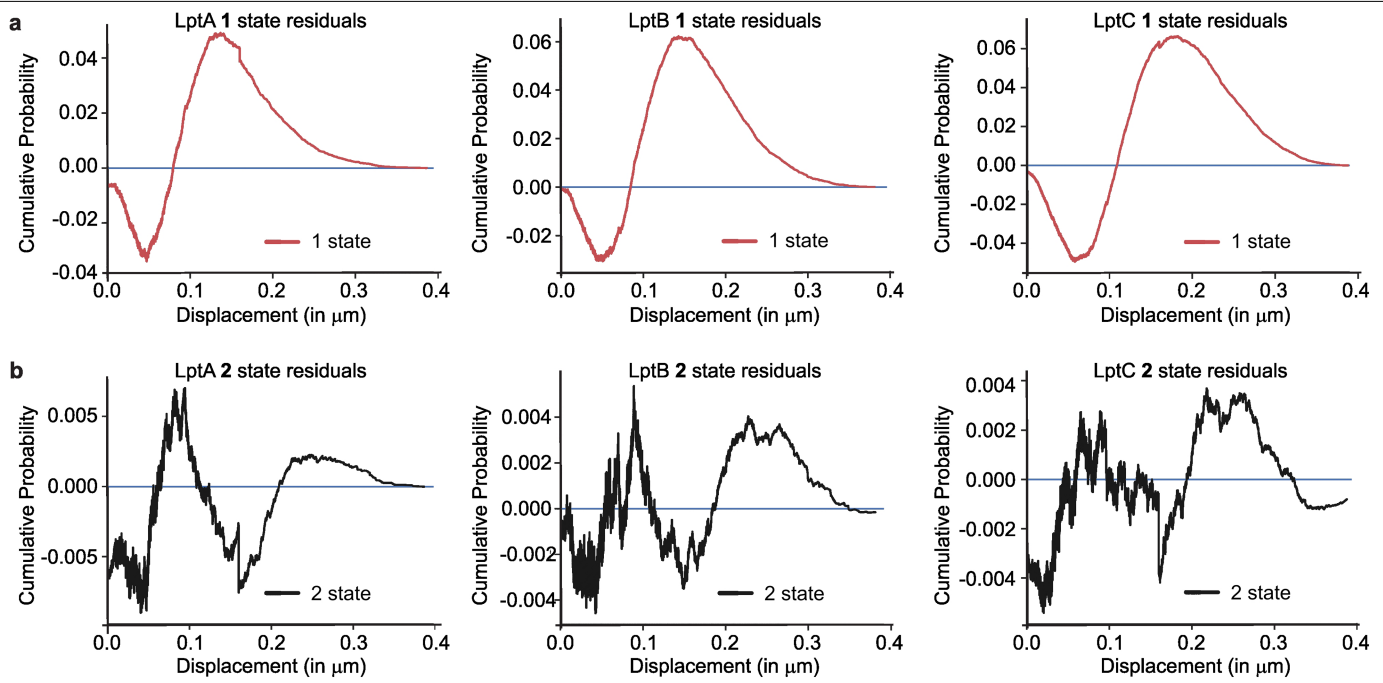
**Extended Data Fig. 2 | Representative trajectories of Halo-tagged LptA, B, C, D, and E.** Trajectories were overlaid over the corresponding phase image. Each trajectory is represented in a different color. The color was chosen randomly.



**Extended Data Fig. 3 | Mean square displacement versus  $\tau$  curves show inhomogeneous dynamics for LptA, B, and C.** 20 randomly sampled MSD versus  $\tau$  plots are shown for trajectories collected for LptA, B, C, E, and D. MSD

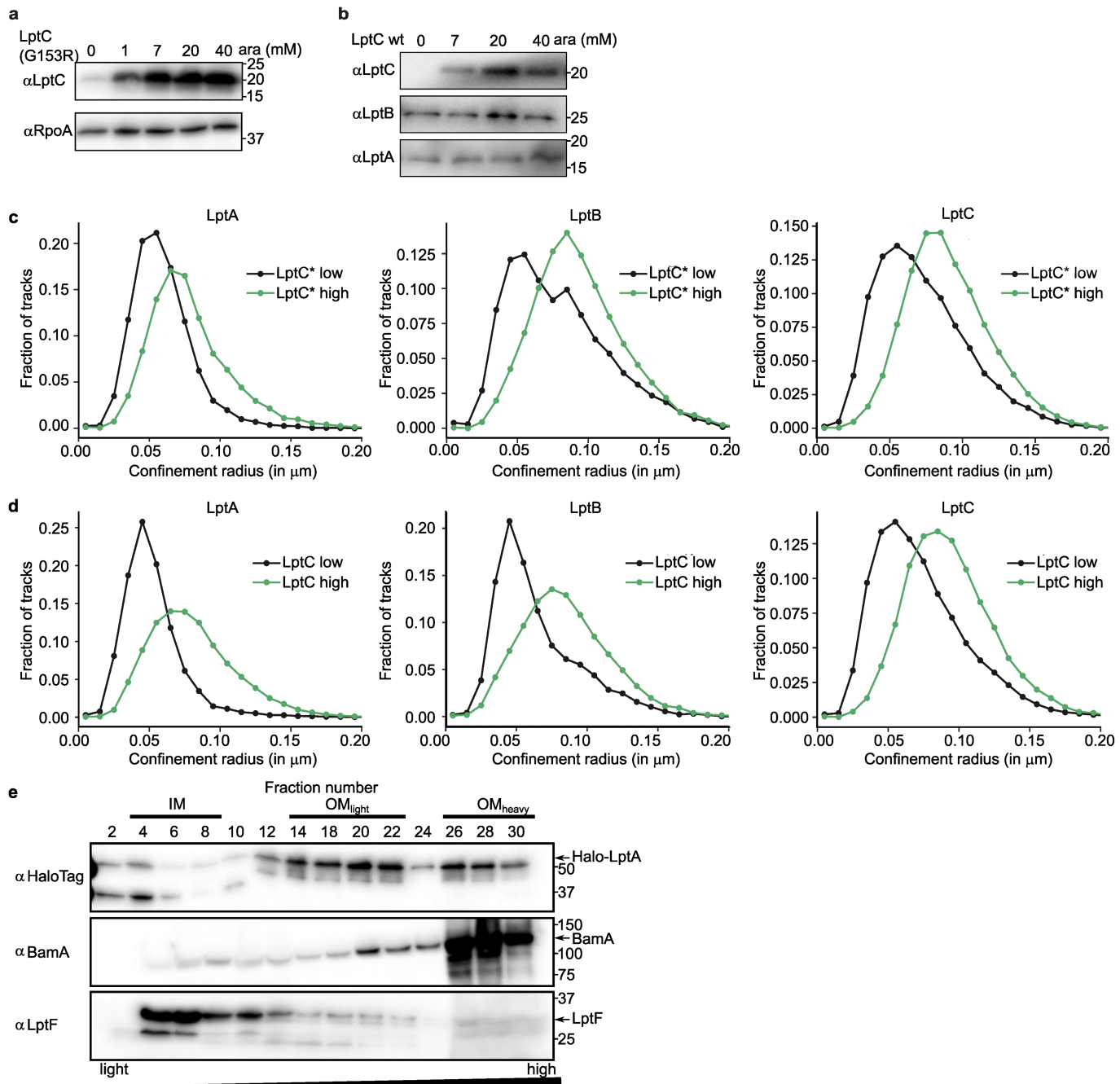
plots for LptA, B and C trajectories show immobile, mobile and switching trajectories. LptD and E show mostly immobile trajectories.

# Article



**Extended Data Fig. 4 | Cumulative distribution function analysis shows two-state dynamics for LptA, B, and C.** Cumulative distribution function of displacements with  $\Delta t = 200$  ms for single-molecule tracks of LptA, B, C, and D were plotted. (Fig. 1f) One state (red line) and two state (black line) dynamic models were fitted to the CDF plots. **a**, Residuals for the one-state dynamic

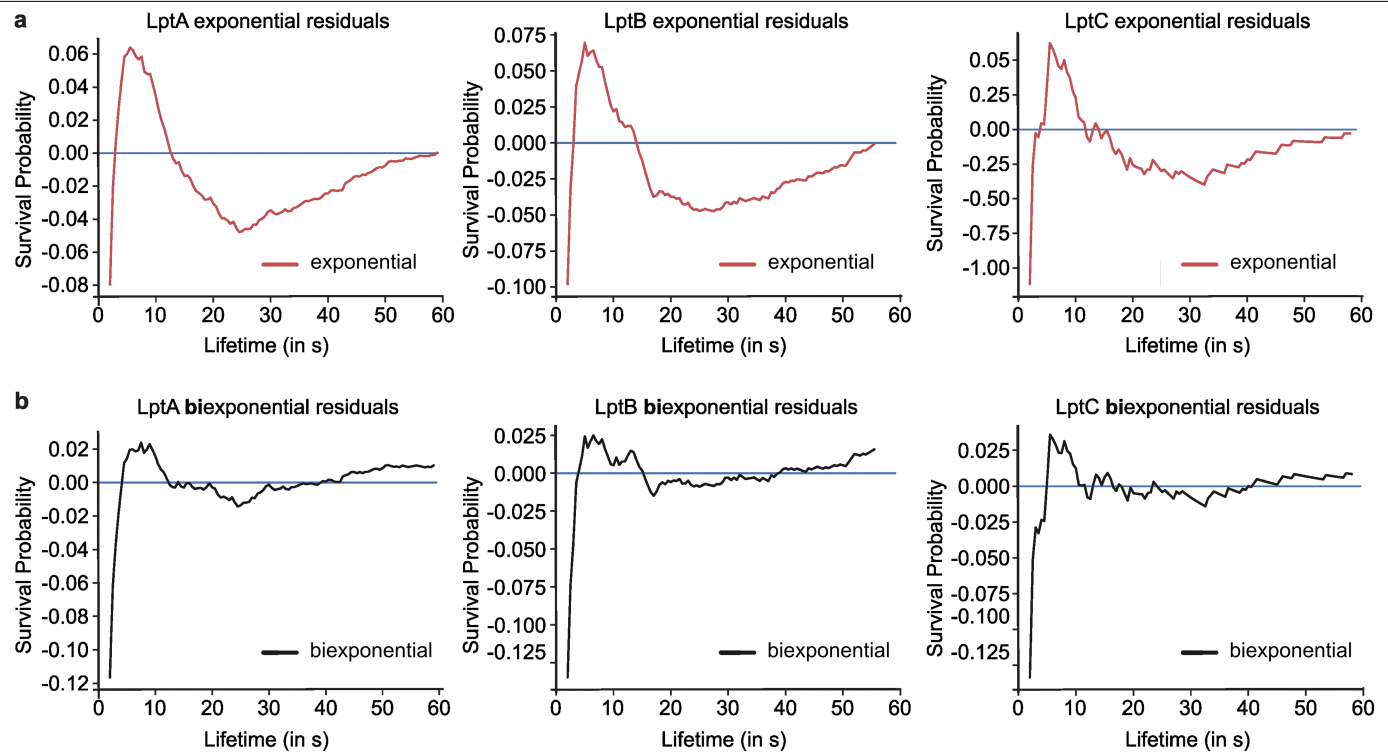
model fit are plotted. **b**, Residuals for the two-state dynamic model fit are shown. For all three proteins, the two-state model resulted in the best fit without over fitting the curve. The results shown are representative of at least two independent experiments.



**Extended Data Fig. 5 | The mobility of LptA, LptB, and LptC changes in response to altering the levels of LptC\* and LptC.** **a**, Immunoblots against LptC and RpoA are shown for LT16 containing pBAD33LptC(G153R) treated with different arabinose (ara) concentrations to express LptC(G153R) (LptC\*) under the same conditions used for imaging. Molecular weight markers are given in kDa. **b**, Immunoblots against LptC, LptB, and LptA are shown for LT16 containing pBAD33LptC treated with different arabinose (ara) concentrations to express wild-type LptC. **c**, Confinement radius plots for LptA, B, and C without inducing (black line, LptC low) and with inducing LptC(G153R) production with 40 mM arabinose (green line, LptC high).  $n = \text{low/high}$ .

LptA:3,552/8,330, LptB:6,773/2,324, LptC:18,938/30,560. **d**, Confinement radius plots for LptA, B, and C without inducing (black line, LptC low) and with inducing overproduction of wild-type LptC with 40 mM arabinose (green line, LptC high).  $n = \text{low/high}$ , LptA:2,371/12,773, LptB:1,311/2,747, LptC:8,864/11,788. **e**, Immunoblots of the fractionation of LptA-Halo containing strain, LT23, are shown. OM<sub>light</sub> is a mixed membrane fraction and contains both IM and OM proteins (including the Lpt bridge), and OM<sub>heavy</sub> contains components fractionating only with the OM<sup>6</sup>. Results shown in this figure are representative of at least two independent experiments.

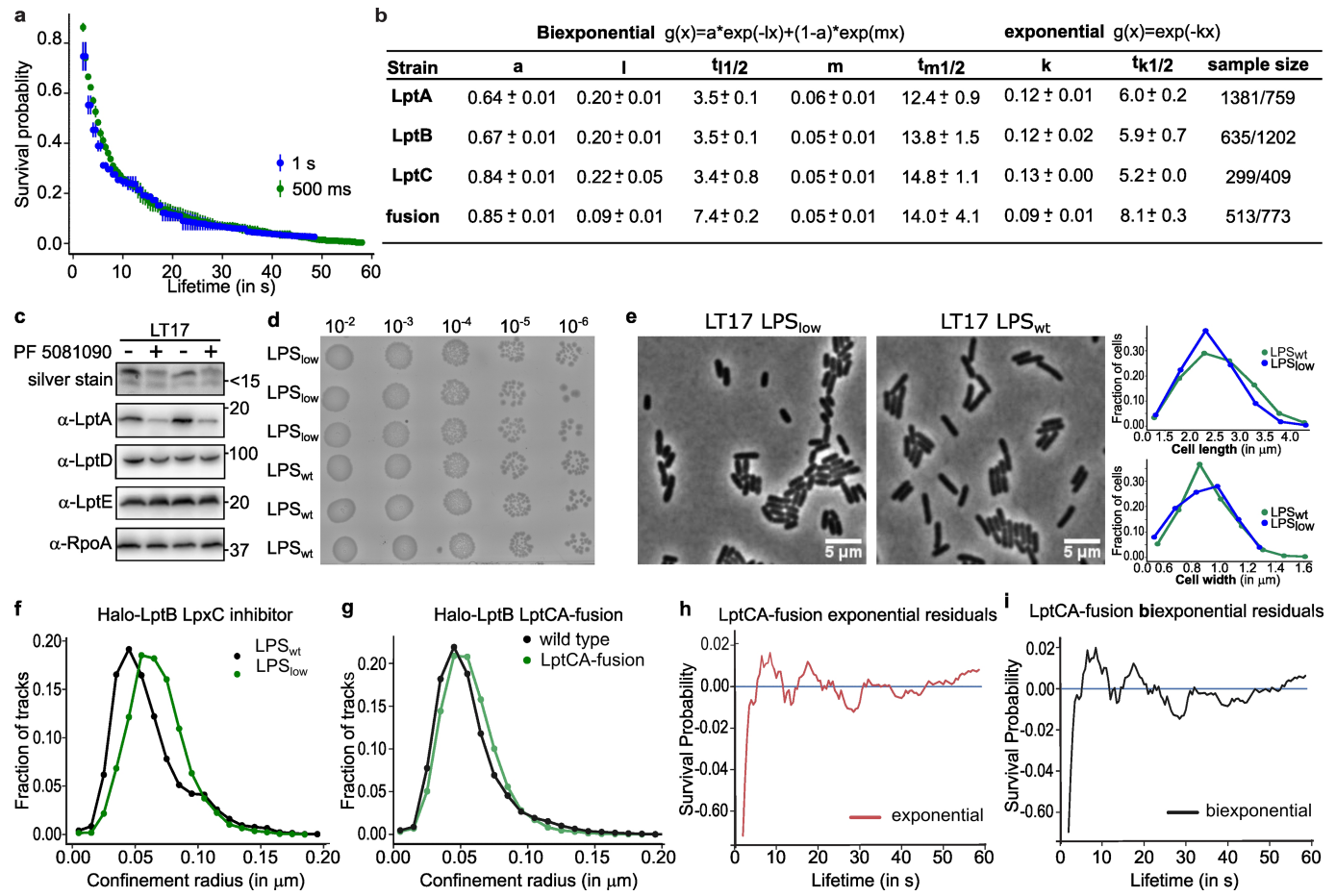
# Article



## Extended Data Fig. 6 | LptA, LptB, and LptC display biexponential decay

**Kinetics.** Single exponential curves (red) and biexponential curves (black) were fitted to the lifetime plots of LptA, B, and C. (line = fit, dots = lifetime data). (Fig. 3b) Fitted values can be found in Extended Data Fig. 7. **a**, Residuals for the

single exponential fits are shown (red). **b**, Residuals for the biexponential fits are shown (black). For all three proteins the biexponential fit resulted in the best fit of the lifetime distribution. Plots are representative of two independent experiments.



#### Extended Data Fig. 7 | Bridge lifetime follows a biexponential decay.

**a**, Bleaching control measurement; Halo-LptC (LT16) lifetime plots measured with 500 ms exposure in 500 ms intervals (green,  $n = 708$ ) compared to 500 ms exposure in 1 s intervals (blue,  $n = 1,186$ ). The average of two independent experiments is shown with the standard deviations (error bars.) **b**, Results for the fitted values of the biexponential and exponential fits to the lifetime data of LptA, B, and C, and for the lifetime data measured for LptB with overproduction of the LptCA fusion. Provided values are the mean of two independent experiments and the standard deviation is given as error. **c**, Silver stain,  $\alpha$ -LptA,  $\alpha$ -LptD,  $\alpha$ -LptE and  $\alpha$ -RpoA blots of LT17 with (+/LPS<sub>low</sub>) and without (-/wt) 0.5X MIC LpxC inhibitor (PF 5081090) treatment are shown. Two replicates are shown. The silver stain detects LPS levels. Molecular weight markers are given in kDa. **d**, Spot dilutions of LT17 on LB agar after LpxC inhibitor treatment

(LPS<sub>low</sub>) are shown in comparison to untreated LT17 (LPS<sub>wt</sub>). Three biological replicates are shown. **e**, Phase images of LT17 with (LPS<sub>low</sub>) and without (LPS<sub>wt</sub>) LpxC inhibitor treatment are shown. Shown images are representative field of views of two independent experiments. Histograms of cell length and width, measured of LT17 cells ( $n = \text{cells/independent experiments}$ , LPS<sub>wt</sub>:300/2, LPS<sub>low</sub>:300/2) with (blue) and without (green) LpxC inhibitor treatment are depicted. **f**, Confinement radius plots for Halo-LptB under wild-type conditions (black line,  $n = 2,110$ ) and with LpxC inhibitor treatment (green line,  $n = 8,145$ ). **g**, Confinement radius plots for Halo-LptB under wild-type conditions (black line,  $n = 3,637$ ) and with overproduction of LptCA-fusion protein (40 mM arabinose, green line,  $n = 3,602$ ). **f, g**, Results are representative of at least two independent experiments. **h, i**, Residuals of the exponential (red, **h**) and biexponential (black, **i**) fit to the LptCA-fusion lifetime distribution (Fig. 4b) are shown.

## Reporting Summary

Nature Portfolio wishes to improve the reproducibility of the work that we publish. This form provides structure for consistency and transparency in reporting. For further information on Nature Portfolio policies, see our [Editorial Policies](#) and the [Editorial Policy Checklist](#).

### Statistics

For all statistical analyses, confirm that the following items are present in the figure legend, table legend, main text, or Methods section.

n/a Confirmed

- The exact sample size ( $n$ ) for each experimental group/condition, given as a discrete number and unit of measurement
- A statement on whether measurements were taken from distinct samples or whether the same sample was measured repeatedly
- The statistical test(s) used AND whether they are one- or two-sided  
*Only common tests should be described solely by name; describe more complex techniques in the Methods section.*
- A description of all covariates tested
- A description of any assumptions or corrections, such as tests of normality and adjustment for multiple comparisons
- A full description of the statistical parameters including central tendency (e.g. means) or other basic estimates (e.g. regression coefficient) AND variation (e.g. standard deviation) or associated estimates of uncertainty (e.g. confidence intervals)
- For null hypothesis testing, the test statistic (e.g.  $F$ ,  $t$ ,  $r$ ) with confidence intervals, effect sizes, degrees of freedom and  $P$  value noted  
*Give  $P$  values as exact values whenever suitable.*
- For Bayesian analysis, information on the choice of priors and Markov chain Monte Carlo settings
- For hierarchical and complex designs, identification of the appropriate level for tests and full reporting of outcomes
- Estimates of effect sizes (e.g. Cohen's  $d$ , Pearson's  $r$ ), indicating how they were calculated

*Our web collection on [statistics for biologists](#) contains articles on many of the points above.*

### Software and code

Policy information about [availability of computer code](#)

Data collection NIS-Elements Microscope Imaging Software (version 5.02.01)

Data analysis Image analysis: Fiji, ImageJ 1.52n  
 Trajectory construction: TrackMate (version 3.8.0)  
 custom code for filtering trajectories, confinement radius analysis and CDF analysis: Python 2.7, numpy (version: 1.16.1), pandas (version 0.17.1) code available at: <https://github.com/Itoerk/Lpt-tracking-code>  
 CDF curve and lifetime fits: lmfit (version 0.9.15)  
 independent two sided t-test: scipy.stats (version 1.2.3)  
 lifetime analysis: Matlab R2020a, Squyres et al. 2020 cited in Methods, <https://bitbucket.org/garnerlab/squyres-2020/src/master/Lifetime%20Analysis/>, Bronson et al., vbFRET, 2009, cited in Methods  
 Bar plots of alpha values, growth curve plots and tracks per cell plots generated with: GraphPad Prism (version 6.01)  
 other plots generated with: Matplotlib (version 2.2.5)  
 Figure production: INKSCAPE 1.2.1

For manuscripts utilizing custom algorithms or software that are central to the research but not yet described in published literature, software must be made available to editors and reviewers. We strongly encourage code deposition in a community repository (e.g. GitHub). See the Nature Portfolio [guidelines for submitting code & software](#) for further information.

## Data

Policy information about [availability of data](#)

All manuscripts must include a [data availability statement](#). This statement should provide the following information, where applicable:

- Accession codes, unique identifiers, or web links for publicly available datasets
- A description of any restrictions on data availability
- For clinical datasets or third party data, please ensure that the statement adheres to our [policy](#)

The data supporting the findings of the study are available in this article and its Supplementary Information files. Raw images and trajectory files are available at [https://dataverse.harvard.edu/dataverse/Lpt\\_tracking\\_data](https://dataverse.harvard.edu/dataverse/Lpt_tracking_data).

## Human research participants

Policy information about [studies involving human research participants](#) and [Sex and Gender in Research](#).

Reporting on sex and gender

NA

Population characteristics

NA

Recruitment

NA

Ethics oversight

NA

Note that full information on the approval of the study protocol must also be provided in the manuscript.

## Field-specific reporting

Please select the one below that is the best fit for your research. If you are not sure, read the appropriate sections before making your selection.

Life sciences       Behavioural & social sciences       Ecological, evolutionary & environmental sciences

For a reference copy of the document with all sections, see [nature.com/documents/nr-reporting-summary-flat.pdf](https://nature.com/documents/nr-reporting-summary-flat.pdf)

## Life sciences study design

All studies must disclose on these points even when the disclosure is negative.

Sample size

Sample sizes were not predetermined. Single molecule data were acquired until the addition of more data would not change the result. This justifies why the used sample size is sufficient. For immuno-blots inferences were not made about a population based sampling, so sample size determination was not necessary. Immuno-blots were not analyzed quantitatively, only qualitatively.

Data exclusions

Confinement radius analysis: trajectories smaller than 5 frames were excluded, trajectories larger than 5 frames were randomly cut to 5 consecutive frames. Data without the minimum frame length were excluded, because analysis all trajectories need to have the same length for the confinement radius.  
 CDF analysis: Trajectories shorter than 4 frames and longer than 150 frames were excluded.  
 Lifetime analysis: lifetimes shorter than 2s and longer than 60 s were excluded.  
 Extremely short or long trajectories/lifetimes likely do not correspond to real single molecule events of proteins. It is accepted practice in the single molecule tracking field to filter trajectories by length to avoid interpretation of junk data.  
 The set filters for data exclusions were determined already before the data analysis.

Replication

None of the results reported could not be replicated. To ensure experimental findings could be reproduced, experiments were replicated as described in the figure captions and Methods.

Randomization

For most performed experiments sample randomization was not relevant. Whenever a bacterial culture was split into treated and control allocation was chosen random.

Blinding

Investigators were not blinded to any data. This is not relevant to the experiments performed in this work. Subjective analysis of results was not needed, so blinding was not necessary.

## Reporting for specific materials, systems and methods

We require information from authors about some types of materials, experimental systems and methods used in many studies. Here, indicate whether each material, system or method listed is relevant to your study. If you are not sure if a list item applies to your research, read the appropriate section before selecting a response.

## Materials & experimental systems

n/a	<input type="checkbox"/> Involved in the study <input checked="" type="checkbox"/> Antibodies <input checked="" type="checkbox"/> Eukaryotic cell lines <input checked="" type="checkbox"/> Palaeontology and archaeology <input checked="" type="checkbox"/> Animals and other organisms <input checked="" type="checkbox"/> Clinical data <input checked="" type="checkbox"/> Dual use research of concern
-----	--

## Methods

n/a	<input type="checkbox"/> Involved in the study <input checked="" type="checkbox"/> ChIP-seq <input checked="" type="checkbox"/> Flow cytometry <input checked="" type="checkbox"/> MRI-based neuroimaging
-----	--

## Antibodies

### Antibodies used

Donkey anti-rabbit HRP secondary antibody was purchased from GE Healthcare (catalog #NA9340V, lot#16801031 and #16955624, 1:10000 dilution).

Sheep anti-mouse HRP secondary antibody was purchased from GE Healthcare (catalog #NA931V, lot#17438421, 1:10000 dilution)

Mouse anti-RpoA primary antibody was purchased from BioLegend (catalog #663104, lot # B252705, 1:2000 dilution)

Anti-HaloTag® sera was purchased from Promega (catalog #G921A, lot#0000463119, dilution 1:1000)

Antiserum against LptA was previously reported and is cited in the Method section (dilution 1:10000)

Antiserum against LptB was previously reported and is cited in the Method section (dilution 1:10000)

Antiserum against LptC was previously reported and is cited in the Method section (dilution 1:2000)

Antiserum against LptD was previously reported and is cited in the Method section (dilution 1:10000)

Antiserum against LptE was previously reported and is cited in the Method section (dilution 1:10000)

Antiserum against LptF was previously reported and is cited in the Method section (dilution 1:20000)

Antiserum against BamA was previously reported and is cited in the Method section (dilution 1:5000)

### Validation

Certificates of analysis for the anti-mouse and anti-rabbit antibodies can be found at <https://www.cytivalifesciences.com/en/us/support/quality/certificates>.

Certificates for the anti-HaloTag® can be found on the Promega website (<https://www.promega.com/resources/certificates-of-analysis/>)

Certificate of analysis for the anti-RpoA antibody can be found at <https://www.biologe.com/en-us/certificate-of-analysis>.

Generation of the anti-LptA antibody is described in reference 40.

Generation of the anti-LptB antibody is described in reference 11.

Generation of the anti-LptC antibody is described in reference 40.

Generation of the anti-LptE antibody is described in reference 6.

Generation of the anti-LptD antibody is described in reference 6.

Generation of the anti-LptF antibody is described in reference 38.

Generation of the anti-BamA antibody is described in reference 59.

The references demonstrate the use of the respective antibodies in Immuno-blotting.